PORTABLE EIS AND SERS SENSING WITH FLEXIBLE SENSORS

BY

JING JIANG

DISSERTATION
Submitted in partial fulfillment of the requirements
for the degree of Doctor of Philosophy in Electrical and Computer Engineering
in the Graduate College of the
University of Illinois at Urbana-Champaign, 2017

Urbana, Illinois

Doctoral Committee:

Associate Professor Gang Logan Liu, Chair
Professor James Gary Eden
Professor Brian T. Cunningham
Professor Huimin Zhao

ABSTRACT

To debottleneck the core development of portable sensing, in this dissertation low-cost, highly sensitive sensors for impedance sensing and surface-enhanced Raman sensing have been designed and tested with mass-manufacturing ability. Starting from silicon-based through-hole impedance with a pre-concentrating function, 100 cells per milliliter detection limit has been achieved. In the following dissertation, the difficult-to-fabricate silicon sensor was replaced by a filter-based sensor, combining with a 3D printed scaffold and low-melting 3D printed filament confining the microfluidic channel, not only the cost was reduced significantly, but the detection limit was further improved by 20 times in the study using the Hook effect and improvement of the equivalent circuit model for paper-based impedance sensing. Further, we developed a Bluetooth-based impedance sensing component that can be used with a smartphone to work with this sensor easily.

On the other hand, we have developed a wafer scale, flexible, polymer-based nano-pillar SERS sensor with an enhancement factor (EF) as high as 4.81×10^8 for the silver-based sensor. This high EF resulted from better adhesion between the substrate and detecting target, as well as the extended hotspots from the dense silver nanoparticles along the nano-pillars. Furthermore, in the following work, we also increased the EF by 3.4 times for a gold-coated sensor which is more stable, and bio-compatible by fine-tuning the distance among nano-pillars. With this ultrasensitive, low-cost, and highly uniformed substrate, the application with a handheld Raman spectrometer for the detection of drugs in wine was also demonstrated.

ACKNOWLEDGMENTS

I would like to first express my sincere gratitude to my thesis adviser, Professor G. Logan Liu, for his helpful guidance and advice, and especially for giving me this opportunity to pursue my degree and conduct research at the University of Illinois at Urbana-Champaign. I would like to thank all the group members in the Liu Nanobionics Laboratory for their indispensable help and discussions. I would like to thank the staff of the Micro and Nanotechnology Laboratory and Materials Research Laboratory for their technical support. Finally I thank my family and friends who gave me comfort and support.

TABLE OF CONTENTS

CHAPTER 1: INTRODUCTION

As with the development of economics, there is a need for increased awareness of the surrounding environment. Harmful foods, pathogens in water, and potential health risks all need solutions for easy and efficient analysis and reporting. With the rapid development of the electronics industry, miniature portable sensing systems are available. In addition, powerful smartphones with various add-ons can also be used as a cost-effective solution for developing a portable sensing system. However, the high-performance sensors now pose a bottleneck in the industry.

In this thesis, we will focus on the development of high-performance impedance sensors for bacteria detection and an ultrasensitive surface enhanced Raman sensor for chemical detection. Further, we will also demonstrate the portable application with those sensors. Both sensors were fabricated with large-scale manufacturing methods and can be produced cost-effectively.

1.1 Introduction of flexible and paper-based sensors

It has been reported that the market for emerging printed and flexible sensor technologies will increase up to $120 million by 2020 from $8 million in 2014.[1] As the internet of things increasingly changes our society, sensors and sensing technologies have entered everyday life. In the coming decade, with increasing interests in healthcare and needs for cost-effective sensing, we can expect the shifting of more research resources to flexible and paper-based sensors.

Recently, flexible electrical and mechanical sensing devices have shown great potential for a variety of applications.[2] Micro- and nano-electronical materials deposited flexible substrates that have achieved different functionalities, including ultra-sensivity, transparency, bendability, and

on-body detectability. One category of flexible sensors is polymer-based devices that have been used for wearable devices, implantable devices, electronic skins, and advanced sensing devices with additional features (self-healing, self-power, and transparency).

Meanwhile, paper is abundant, available in different thicknesses, biodegradable, environmentally friendly, and lightweight. Its porosity and hydrophilicity can be utilized for a natural platform for microfluidic channel fabrication.[3] The development in multiple areas has benefited the paper-based sensing technology, so that paper-based assays have been widely applied in different areas, including the food industry, medicine, aquaculture/agriculture, security environmental safety, bioanalysis, bacteria detection, and chemical contaminants. At the early stage, paper-based sensors were mostly used for qualitative or semi-quantitative analysis. Currently, quantitative analytical methods have been used for paper-based sensors including colorimetry, fluorescence, electro-conductivity, and electrochemistry.

Besides the versatility, low-cost, and simplicity of the flexible or paper-based sensors, nowadays, with highly integrated external devices such as smartphones, wearable technology, or imaging devices, optical drives, and strip readers, these sensors can be used in many more scenarios. In addition, the advances in nanotechnology have also increased the performance of the flexible sensors.

1.2 Introduction of EIS sensing

Electrochemical impedance spectroscopy (EIS) measures the dielectric properties of a medium as a function of frequency. It is based on the interaction of an external field with the electric dipole moment of the sample, which is often expressed by permittivity. EIS reflects electronic and physical properties of an electrochemical system over a wide frequency range, including: diffusion coefficients, absorption mechanism, capacitances, charge transfer resistances, and electron

transfer rate constants.[4] EIS measurement does not require special reagents and is a good candidate for label-free detection.

A monochromatic signal

$$v(t) = V_m \sin(\omega t) \tag{1.1}$$

is applied to a cell and the resulting steady-state current

$$i(t) = I_m \sin(\omega t - \theta) \tag{1.2}$$

where ω is the frequency of the signal and θ is the phase difference between the applied voltage and the stimulated current which is zero for purely resistive behavior. The complex-valued impedance $Z(\omega)$ has magnitude V_m/I_m and phase θ.

Since most real electrode-material systems are nonlinear, EIS measures tend to show strong nonlinear behavior, especially in their interfacial response, when applied voltages or currents are large. However, when potential difference amplitude V_m is less than the thermal voltage,

$$V_T \equiv \frac{RT}{F} \equiv \frac{kT}{e} \tag{1.3}$$

At about 25 mV at 25 ℃, it can be shown that the basic differential equations which govern the response of the system become linear. Here k is Boltzmann's constant, T the absolute temperature, e the proton charge, R the gas constant, and F the Faraday constant.

Considering the application, EIS has been applied widely in the bio-sensor area including point of

care testing, public safety detection, health monitoring, and cell counting, since it has the advantages of supporting label-free detection, results in no damage to the biomolecular layer, has low-cost and small-sized sensors, and provides multiplexing capabilities. However, the current challenges are the reproducibility of the sensors, limited affinity and selectivity of sensing targets, and the complexity of the readout setup.

As the rapid increase of the flexible biosensor market shows in Fig. 1.1, it is expected that the impedance-based biosensor also has a great potential in the future. The impedance-related sensing technique has been applied to E. Coli detection,[5] HIV diagnostics,[6] and biomolecule detection with nano-pore structure[7]. Most biosensors require a label attached to the target, during readout the amount of the label is detected. Under the assumption that the label concentration corresponds to the number of bound targets, the targets can be quantified. Labels can be magnetic beads, active enzymes that are easily detectable, or fluorophores. However, labeling a biomolecule can change its properties.

Instead, the impedance measurement is excited by a small voltage perturbation, thus the biomolecule will not be destroyed. The cost of a sensing chip for impedance is very low. Traditional micro-meter level photolithography can finish the mass-production of the chip at a low cost and high signal-to-noise ratio. At even lower cost, sensor chips of a large feature size can be fabricated with a shadow mask so that they can be produced in one step. Considering the challenges of the reproducibility of the sensor, the affinity and selectivity, and bulk readout setup, we used different methods to solve the problems of above challenges in the following chapters.

The smartphone is the latest generation of cellphones which have excellent built-in features including digital cameras, multicore processors, touch screens, fast network connection, and GPS locating capability.[8] Unlike its predecessors, current smartphones have impressive performances

capabilities including high image resolution, advanced computing power, and supporting apps for different functionalities. Built-in Bluetooth also supports the connectivity of cellphones with many different peripherals for assorted biosensors and bioelectronics systems. On one side, the smartphone provides a well-designed user interface with which users can operate the associated sensing system. Meanwhile, the sensing result can be well documented and analyzed by the smartphone while the user can receive diagnostic information and health suggestions combined with medical big data. On the other side, the popularity of smartphone usage enables more users to have access to low-cost detection since the sensing devices using a smartphone as their user interface lowers the cost, thereby increasing the affordability and usability significantly.

Until today, as shown in Fig. 1.2, the smartphone has been used as a sensing platform for different purposes. The electrochemical detection system performs cyclic voltammetry, chonoamperometry, differential pulse voltammetry (DPV), square wave voltammetry (SWV), and potentiometry, all of which have comparable performance with commercial potentio-stat at a certain voltage and current range has been reported by Nemiroski et al. in 2014.[9] Lillehoj et al. (2013) used an amperometric biosensor system for PfHRP2 detection. The system consisted of a smartphone, a disposable microfluidic chip, and an embedded circuit. The phone can communicate with the circuit via an audio jack, control the fluid and bio-sensing signal on the microfluidic chip, and finally display results on the screen.[10] Delaney et al. (2013) combined the paper-based microfluidic, potentiometry measurement capability with an audio jack, and used colorimetry detection from the phone camera for their sensing purpose.[11]

In the following text, we will introduce our preliminary results from this PhD work with smartphone-based bacteria sensor, smartphone-based TNT sensor, and proposed research for smartphone-based blood cell counter with an impedance measurement and paper-based fluidics sensor.

1.3 Cells as electronics

A bacterial cell wall has a negative charge. In Gram positive bacteria, the reason of this negative charge is the presence of teichoic acids linked to either the peptidoglycan or to the underlying plasma membrane. These teichoic acids are negatively charged because of the presence of phosphate in their structure. The Gram negative bacteria have an outer covering of phospholipids and lipopolysaccharides. The lipopolysaccharides impart a strongly negative charge to the surface of Gram negative bacterial cells.[12]

Thus, bacteria carry positive or negative ions on their membrane. Overall, they can be equivalent as super-sized ions. Under the application of an electric field, cells can drift close to the electrodes and pass some of their ions to the electrodes. Though there is still a resistance for ions to be converted to electrons, the corresponding charge transfer resistance will be lower at a high concentration of bacteria.

Resistive property: The ion channels across cell membranes resist the movement of electrical charges from passing through. This is mainly due to collisions with the channel wall where energy is given up as heat. Although equivalent voltage sources also exist, the DC voltage sources will not affect AC impedance sensing. Here we will skip the detailed discussion of the topic.

$$R_{th} = \frac{1}{\frac{1}{R_K} + \frac{1}{R_{Na}} + \frac{1}{R_{Cl}}} \tag{1.4}$$

Capacitive property: Capacitance occurs whenever electrical conductors are separated by an insulating material. The cytoplasm and extracellular fluid are the electrical conductors and the lipid bilayer of the membrane is the insulating material. Capacitance for a cell membrane is

approximately 1 mF = cm^2. Membrane capacitance implies that ions do not move through the membrane except through ion channels.

Thus, when performing result analysis, we can build different circuit models to better understand and more clearly present our results.

1.4 Raman spectroscopy and surface-enhanced Raman scattering

Raman spectroscopy is a spectroscopic technique to observe rotational, vibrational, and other low-frequency modes in a system.[13] It is commonly used in chemistry to provide a fingerprint of molecules to be identified. It relies on the inelastic scattering of between monochromatic light from a laser and the functional groups of the molecules. The light interacting with phonons (molecular vibrations) results in the energy of the laser photons being shifted up or down. The shift in energy gives information about the vibrational modes in the system. Usually, a laser beam illuminates a sample. Electromagnetic radiation from the illuminated spot is collected with a lens and sent to an optical system. The light with wavelength equal to that of the incident wave (Rayleigh scattering) is filtered out and the rest is projected onto a detector with a grating and a CCD detector.

However, spontaneous Raman scattering is a weak phenomenon and the resulting spectrum is blended with intense Rayleigh scattered laser light. Mostly, researchers can get weak Raman signals only when large quantities of samples, high power of the incident laser beam, and long exposure time are applied.

Because surface-enhanced Raman spectroscopy (SERS) gives a much stronger Raman scattering, it is the focus of this dissertation. Normally SERS is done in a gold or silver colloid or substrate containing gold or silver. Because Raman intensities are proportional to the electrical field, there

is a significant increase in the measured signal.

Metal-coated nano-pillars have SPR (surface plasmon resonance). Here we will introduce SPR briefly. A plasmon is the collective excitation of the electron gas of a conductor. A surface plasmon occurs if the excitation is confined near the surface. It can be either propagating or localized. Under conditions of surface plasmon excitation, the electromagnetic field of the light at the surface can be substantially enhanced. Both the incident laser field and the scattered Raman field under this condition constitute the SERS mechanism. For example, for a metal sphere in an external electric field, if the radius is much smaller than the wavelength of light, the electric field can be approximated by the Rayleigh scattering model. The field induced at the surface is related to the field of the laser for eqn. (1.1), where $\varepsilon_1(\omega)$ is the frequency-dependent, complex dielectric function of the metal and ε_2 is the relative permittivity of the ambient phase. Resonance occurs at the frequency when $\mathrm{Re}(\varepsilon_1) = -2\varepsilon_2$. Excitation of the surface plasmon greatly increases the local field experienced by a molecule absorbed on the surface of the particle. As the particle not only enhances the field of the incident laser but also enhances the Raman scattered field, a small increase in the local field produces a large enhancement in the Raman scattering. Overall enhancement scales roughly as the fourth order of the electrical field.[14]

$$E_{induced} = \left({\varepsilon_1(\omega) - \varepsilon_2} \Big/ {\varepsilon_1(\omega) + 2\varepsilon_2} \right) E_{laser} \qquad (1.5)$$

With the contribution of SPR, SERS provides a substantially stronger signal than the normal Raman scattering does. For example, from the work of Kahraman et al. (2013), the normal Raman signal of 0.1 M rhodamine 6G (R6G) is only 1/10 the intensity of the SERS signal of 10^{-6} M R6G.[15] Thus, SERS in this work amplified the signal intensity by about 10^6 so that targets with a very low concentration can be identified.

In the following dissertation, we will demonstrate our ability to integrate black silicon features which are random nano-pillar structures to assorted micro-structured silicon devices. Then we will investigate the abilities of SERS with these structures coated with silver.[16]

1.5 Figures

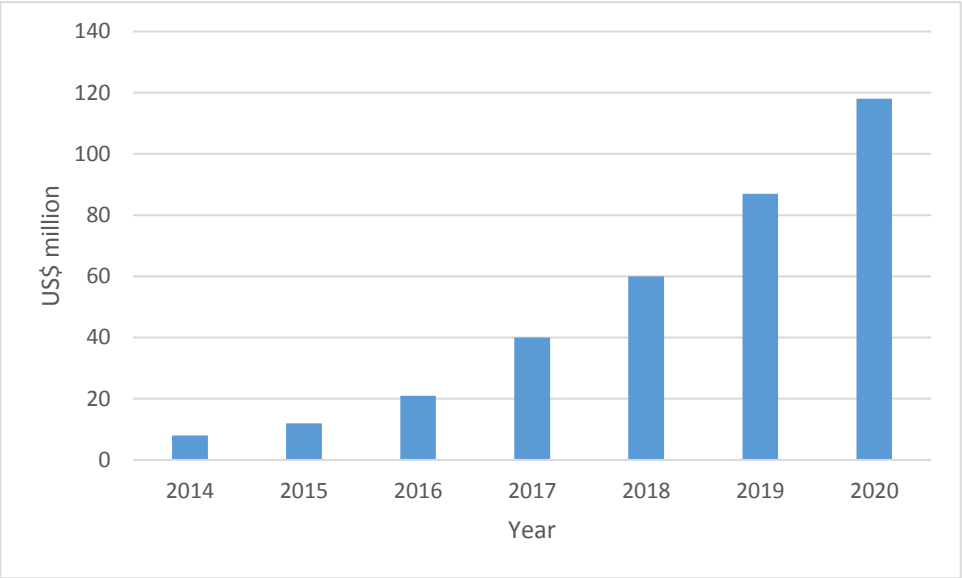

Figure 1.1 Market forecast (at sensor module level) for emerging printed and flexible sensor technologies.[1]

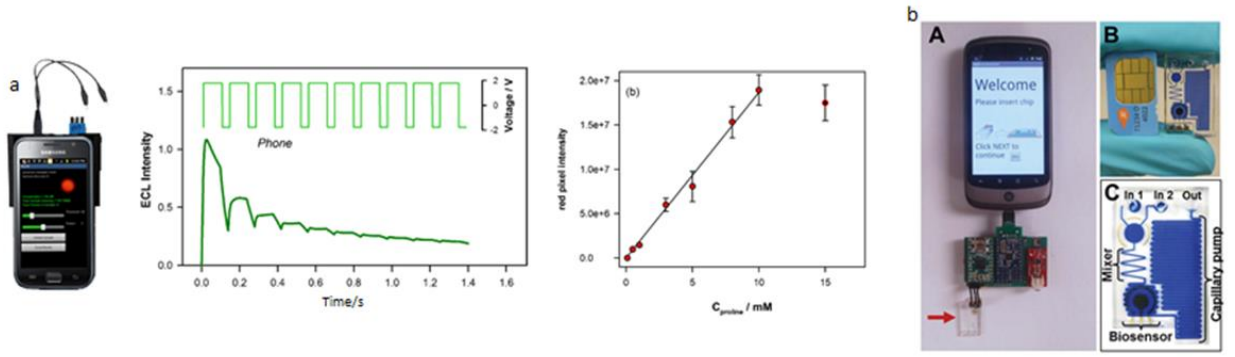

Figure 1.2 (a) Phone based potentio-static control with paper-based microfluidics sensor.[11] (Reprinted from J. L. Delaney, E. H. Doeven, A. J. Harsant and C. F. Hogan, *Anal. Chim. Acta*, 2013, **790**, 56–60, with permission from Elsevier.) (b) Smartphone based microfluidic sensor for PfHRP2 detection.[10] (Reprinted from P. B. Lillehoj, M.-C. Huang, N. Truong and C.-M. Ho, *Lab Chip*, 2013, **13**, 2950, with permission from Royal Society of Chemistry.)

CHAPTER 2: BACTERIA PRE-CONCENTRATING IMPEDANCE SENSING SYSTEM

2.1 Introduction

With the improving life quality in many developed and developing countries, citizens are more concerned about food and water safety and eager to know whether their drinking water or food are contaminated by nitrate,[17] harmful bacteria,[18] or heavy metal ions.[19] Some species of Escherichia Coli (E. Coli) and Salmonella bacteria have been known to have caused serious food and water contamination issues which can severely threaten civilians' health conditions.[20] In order to quantify the amount of bacteria quickly, researchers have developed fluorescence detection techniques and DNA-biosensors to count E. Coli[21] for various bacteria detections. However, fluorescence detection needs dye labeling[22] which requires high expense and professional training for operation. DNA-biosensor is also required to perform Polymerase chain reaction (PCR) as the first step[23] which is a complex procedure that requires sophisticated facilities. So researchers also invented a series of label-free detection methods including quartz crystal microbalance (QCM),[24] microfluidic[25] and electrochemical methods.[18] Some of the techniques can detect the bacteria rapidly and accurately, however most of these detection methods have to be performed in specialized laboratory environments with the assistance of sophisticated equipment.

Among these detection techniques, the electrochemical impedance spectroscopy (EIS) method is able to elucidate the electronic and physical properties of electrochemical systems including diffusion coefficients, adsorption mechanisms, capacitances, charge transfer resistances, and electron transfer rate constants. Due to its sufficient sensitivity, simplicity and cost-effectiveness,

EIS has been increasingly applied in bio-sensing with numerous methods in the past few years.[26] It has also been implemented as a label-free detection tool for quantification of bacteria with minimal sample preparations.[27] Additionally, by coating the electrodes with different antibodies, people used EIS method to detect different pathogens like E. Coli O157.[28] However, high limit of detection and low sensitivity have prevented the application of EIS from being used practically in-field as a bacteria sensor. Meanwhile, microfluidic chip-based measurement platforms which are affordable, portable and accessible to the public[29] have not been developed yet. Fortunately, as the smartphone is becoming more popular in our daily lives, researchers have started to explore the possibilities to make use of this powerful and portable platform for biological sensing.

In 2012, the smartphone became more prevalent in the U.S. market with 115.8 million users accounting for ~37% of U.S. population, expected to rise to ~61% by 2016. With the integration of GPS, powerful CPU, touch-screen displays, internet connection capability, and an intelligent operating system, smartphones are able to provide extensive user-friendly services. Affordable smartphone peripheral devices with sensing capabilities will immensely help citizens to learn more environmental information like air and water quality at any location and at any time.[30] Bacteria sensing information collected by the phones can also be transmitted to cloud computing sites through 3G/4G networks for further data processing and establish a participatory water-borne bacteria sensing map on the internet for information broadcasting.

In this chapter, we report the design, fabrication and integration of a low-cost, handheld, and sensitive microfluidic EIS bacteria pre-concentrator and sensor based on a smartphone through wireless connection. It enables smartphone users to detect the density of as few as 10 E. Coli cells per milliliter of water. Our integrated microfluidic sensor has interdigitated sensing electrodes on a micro-hole array silicon substrate and a sensing microfluidic chamber bounded by a nano-porous filter paper which is also used to pre-concentrate bacteria in sample solutions. A

specifically designed impedance network analyzer chip with a micro-controller together performs EIS measurement and analysis. An Android application program (App) has been developed to enable recording and visualization of testing results as well as control of the sensor electronics. The real-time measurement data will be transmitted to a smartphone by a Bluetooth circuit module.

2.2 Methods

2.2.1 Principle and design

The principle of our miniaturized bacteria sensor is EIS theory which has been developed and applied in bacteria quantification[30,31] for more than a decade. According to the Randles model, the equivalent circuit includes ohmic resistance (R_s) of electrolyte, Warburg impedance (Z_w) resulted by the diffusion of ions from bulk electrolyte to the interdigitated electrodes, electron-transfer resistance (R_{et}) and double-layer capacitance (C_{dl}) shown in Fig. 2.1 (a). R_s and Z_w represent the features of the electrolyte solution diffusion at the probe, while C_{dl} and R_{et} depend on the insulating and dielectric properties at the interface of electrolyte and electrodes and are affected by the property change occurring at the electrode interface.

The distribution of bacterial cells between the interdigitated electrodes affects the interfacial electron-transfer kinetics and thereby increase or decrease the electron-transfer conductivity in electrolyte environment. R_{et}, the electron transfer resistance, is a parameter that can be observed at higher frequencies corresponding to the electron-transfer-limited process and can be measured as the diameter of the semicircle portion in the Nyquist plot in Fig. 2.1 (b). The intercept of the semicircle with the Z_{re} or the real axis at high frequency is equal to R_s. The linear part in Fig. 2.1 (b), which is the characteristic at lower frequencies, represents the diffusion-limited processes.

The design of multi-stage filtering is comprised of one layer of silicon chip having a large array of through holes with diameter of 10 microns and one layer of nano-porous filter paper with submicron pore size. Figure 2.1 (c) shows the cross-sectional view of the integrated bacteria sensor. When the sample solution containing bacteria is injected from the bottom inlet, large particles in the solution will be blocked by the silicon filter while bacteria of our interest can go through the 10-micron-in-diameter silicon holes and are then blocked by the nanoporous filter, staying in the microfluidic sensing chamber. The pre-concentrated bacterial cells distributed around the interdigitated electrodes are subject to impedance sensing. The entire integrated components are packaged by Polydimethylsiloxane (PDMS) material. Figure 2.1 (d) shows the concept design of our packaged device. Users can take a certain amount of a suspicious water sample which may contain bacteria into a syringe, and then inject the liquid through the channel as shown in Fig. 2.2 (a). Since all the bacteria are blocked by the filter and only 30 μL of liquid remains as a result of our geometric design, this sensor package allows users to pre-concentrate the bacteria solution before the measurement. The capacities of most standard syringes range from 1 mL to 60 mL, so we can pre-concentrate the bacteria by 10 to 2000 folds after excess liquid leaves the chamber from the outlet. Thus, our detection limit can be improved to as low as 10 bacterial cells per milliliter. The actual miniaturized bacteria sensor package is as large as one U.S. quarter-dollar coin as shown in Fig. 2.2 (b).

2.2.2 Wireless system for the sensor

A schematic diagram illustrating the main components of the wireless system is shown in Fig. 2.2 (c). Our wireless sensor system has been designed applicable for most of Bluetooth transceiver as well as for Android phones. Our system includes an Android cellphone (HTC ONE X), a Bluetooth shield (Seeed SLD63030P), a micro controller (Arduino), a chip for impedance

converter network analyzer (AD 5933), and our packaged sensor. An Android App has been developed for users to set the start/end frequencies and the frequency sweeping step size in impedance analysis. The “Connect” button allows the cellphone to connect the sensor through the Bluetooth. The benefits of Bluetooth connectivity include efficient power consumption of less than 10 mW[32] and standardization for smartphones and computers. Then the Arduino microprocessor board generates corresponding commands according to the input parameters from the smartphone and asks the AD 5933 chip to send out sinusoidal signals to the bacteria sensor. Depending on the concentration of the bacteria, the corresponding signals acquired by the AD 5933 chip are sent back to the smartphone through the Arduino board and the Bluetooth shield. After this process completes, the smartphone App plots the impedance value with respect to frequency on the screen as shown in Fig. 2.2 (c). It can also calculate a calibration curve after measuring several standard bacterial solutions, and then users can measure the bacterial concentration of an unknown sample. Figure 2.2 (d) illustrates the basic diagram of the wireless LCR sensing platform which communicates with the mobile phone through the Bluetooth and can drive our packaged bacteria sensor to quantify bacteria. The micro-controller writes commands to the impedance converter chip and passes the start\end frequency and sweeping step data from the cellphone to the chip. The on-chip oscillator module of impedance converter generates corresponding sinusoidal waves as the input signal of the bacteria sensor. The output signals of the bacteria sensor containing attenuated amplitude and phase change information are analyzed by an on-chip digital signal processor with 1024 points discrete Fourier transform. Real and imaginary parts of the results are sent to the micro-controller for converting into impedance and phase information. Eventually, these results are transmitted back to the cellphone through the Bluetooth and displayed on the smartphone screen. After calibration by standard solutions, our platform and app can provide accurate quantification information for the tested bacterial solution.

2.2.3 Sensor microfabrication

The sensing part of miniaturized bacteria sensor is a pair of interdigitated electrodes fabricated on a piece of silicon chip with micro-scale through-hole arrays. Because interdigitated microelectrodes have advantages over conventional electrodes for analytical measurements including a high signal-to-noise ratio, low resistance, small solution volumes requirement and rapid attainment of steady state, we adopt this design as the sensing part of our sensor in this dissertation. The top view image of this part is shown in Fig. 2.3 (a). The diameter of the holes is 16 μm. The spacing between the electrodes is 20 μm while the width of the electrodes is 10 μm. Starting from a 380 μm thick silicon wafer (UniversityWafer, Inc. 1815, p type, Boron doped, 4" 5~10 Ohm), 1 μm of SiO_2 was deposited with Plasma-Enhanced Chemical Vapor Deposition system (PlasmaLab) first at 300 ^{o}C. Then, a layer of 100 nm Al_2O_3 which would be used as a hard mask for through holes was deposited uniformly and firmly on the SiO_2 layer by Atomic Layer Deposition (ALD) system (Cambridge NanoTech) at 250 ^{o}C as what Fig. 2.3 (b)① shows. Al_2O_3 deposited by ALD has been proved to be a good mask for fluoride-based Si deep reactive ion etching (DRIE) in our experiment. 100 nm Al_2O_3 allows ~200 um Si to be etched through. Then, photolithography and patterning were done with AZ 5214 photoresist and Karl Suss aligner as shown in Fig. 2.3 (b)②. The 15 nm of Ti for adhesion and 200 nm of gold were deposited by electron beam evaporation (Temescal). After the metal on the photoresist was lifted off by acetone bath, the gold layer on the exposed region remained as the pair of interdigited electrodes as shown in Fig. 2.3 (b)③. After the fabrication of electrodes, another layer of micro-hole array mask was aligned and patterned. The holes were located between the electrodes and were designed for the bacteria to pass through while blocking big dirt particles in water samples. Buffered oxide etcher (1:10 HF: NH_4F) was applied to etch the Al_2O_3 and SiO_2 (Fig. 2.3 (b)④, Fig. 2.3 (b)⑤) hard masks. Then, XeF_2 etching (XACTIX) was performed on the back side of the silicon

on the exposed part to thin down the silicon by half of its total thickness so that the micro-holes could be etched through by Bosch process with STS Advanced Silicon Etcher (Fig. 2.3 (b)⑥, Fig. 2.3 (b)⑦) for only around 1.5 hrs.

2.3 Result and discussion

2.3.1 Concentration measurement

E. Coli samples were provided by the Institute for Genomic Biology from the University of Illinois at Urbana and Champaign (UIUC) with the strain number of DH5a. The E. Coli stock solution was centrifuged and rinsed with deionized water twice and diluted by 10, 100 and 1000 times respectively. The E. Coli concentration for the stock solution is about 10^7 ml^{-1} measured by hemocytometer.

The prepared E. Coli solution was injected into our device in the order of increasing concentration. To test the performance of packaged sensor electronics, a commercial LCR meter, Agilent 4284A, was used as the benchmark to measure the bacteria impedance by sweeping the signal frequency from 1 kHz to 1 MHz with a step size of 1 kHz.

Figure 2.4 (a) shows the Nyquist plot of the bacteria impedance measurement results. At low frequency the bacteria sensing is mass transfer controlled, while at high frequency the bacteria sensing is kinetics controlled. In the kinetics controlled region, the diameter of the semicircle on the Nyquist plot indicates the electron transfer resistance R_{et}. We found the relationship between bacteria concentration and electron transfer resistance in logarithmic form in Fig. 2.4 (b). The fitting formula is:

$$\log R_{et} = -0.153 \log C_{bac} + 4.187 \quad (2.1)$$

The electron transfer resistance R_{et} and bacteria concentration C_{bac} could be related by Randles equivalent circuit of electrochemical impedance spectroscopy. According to Fig. 2.1 (a) and (b), at high frequency, the Warburg impedance becomes negligible compared with R_{et}. Therefore the Faradaic impedance could be simplified to only electron transfer resistance R_{et}. Due to charge-transfer kinetics, the electron transfer resistance could be defined as:

$$R_{et} = \frac{RT}{nFi_0} \quad (2.2)$$

Here R is gas constant; T is absolute temperature; n is the number of transfer electrons; F is Faraday constant and i_0 is exchange current. In the theory of electrode kinetics, the exchange current at equilibrium condition could be defined as

$$i_0 = FAk^0 C_O^{*\,1-\alpha} C_R^{*\,\alpha} \quad (2.3)$$

k^0 is the standard heterogeneous rate constant. Since E. Coli is negatively charged in a neutral pH environment,[33] we can assume that electrons spread out on the surface of bacteria so that the movement of cells contributes to the electron transfer current. The concentration of bacteria could be expressed as

$$C_{bac} = C_O^{*\,\beta_1} = C_R^{*\,\beta_2} \quad (2.4)$$

The exchange current could be simplified as:

$$i_0 = FAk^0 C_{bac}{}^{\beta} \tag{2.5}$$

In this case, the relation between electron transfer resistance and bacteria concentration could be expressed as: $R_{et} \propto C_{bac}{}^{-\beta}$. Figure 2.4 (b) displays this relationship from experimental data and parameter β equals 0.153, which is consistent with theoretical derivation. Furthermore, in the condition of high frequency, the semicircle in the Nyquist plot could be expressed as the function of real part (Z_{Re}) and imaginary part (Z_{Im}) as:

$$(Z_{Re} - R_s - \frac{R_{et}}{2})^2 + Z_{Im}{}^2 = (\frac{R_{et}}{2})^2 \tag{2.6}$$

The imaginary peak point on the semicircle satisfies the relationship:

$$\omega = {}^{1}/_{R_{ct}C_{dl}} \tag{2.7}$$

ω is the voltage frequency while C_{dl} is the double-layer capacitance. By considering the Gouy-Chapman double-layer model, which involves a diffusion layer of charge in the solution, the double-layer capacitance can be related to bacteria concentration in logarithmic form as linearity. This relationship could be proved by the fitting curve in Fig. 2.4 (b).

Here is one issue worth noting. In most other journal articles for bacterial detection,[34] the electron-transfer resistance (R_{et}) increases as the concentration of bacteria increases. However, our testing data show that R_{et} decreases as the bacteria concentration increases. To explain this

phenomenon, we need to review Fig. 2.1 (a) where R_s is the ohmic resistance of the electrolyte. In other cases, researchers used a conductive electrolyte like 1X Phosphate-buffered saline (PBS) whose high conductivity is associated with low R_s. In those models,[34] antibody treated electrodes trapped bacterial cells close to the electrodes and the double layer of lipid bilayer membrane of the cells retarded the electron transfer in the electrolyte. As a result, R_{et} increased while the concentration of cells increased. In our case, deionized (DI) water (18 MOhm) was applied to dilute E. Coli bacteria after centrifuging and rinsing from culture medium before testing, since E. Coli at around a neutral pH environment carries charge,[33] higher concentration of E. Coli induced resistance R_{et} lower than the resistance of electrolyte, R_s.

The reason we used DI water as the background solution to detect the concentration of bacteria is that our project investigated a new method for direct detection and quantification of bacteria on a mobile detection platform in no need of pretreating field water samples, like centrifuging and diluting with 1X PBS and other redox molecule additives like $[Fe(CN)_6]^{3-}/^{4-}$. The current result is a proof of concept to find the correlation between bacteria concentration and EIS in natural waters.

2.3.2 Smartphone software application

The software was developed on an Android operating system. Implemented with multiple functions of sending sensor control commands, receiving data and plotting, this software is able to remotely control micro-controller (Arduino) through a Bluetooth Shield transceiver board. Connected with the miniaturized bacteria sensor, the smartphone App is able to implement the same functions as a commercial LCR meter does. The user interface of the App is shown in Fig. 2.2 (c).

In order to characterize the sensing capability of the smartphone bacteria sensor system, we have performed the tests with different concentrations of E. Coli solutions and measured impedance spectra by sweeping the frequency from 2 kHz to 100 kHz, as shown in Fig. 2.5 (a). Figure 2.5 (b) and (c) show the magnified chart of Fig. 2.5 (a). We diluted the stock bacteria solution into different concentrations and used a 60 ml syringe to let 60 ml of calibration sample solutions with the cell concentrations of 10 ml^{-1}, 100 ml^{-1}, 1,000 ml^{-1}, and 10,000 ml^{-1} to pass through the sensor. A Nyquist diagram was plotted on the smartphone screen as the thin lines in Fig. 2.5 (b). Then the program can automatically extract the R_{et} value by calculating the peak imaginary resistance from the curve in Fig. 2.5 (b) and plot the R_{et} versus E. Coli concentrations diagram as shown in Fig. 2.5 (c). A blue fitting curve has been derived as, where x is the concentration of E. Coli and y is the imaginary impedance peak, R_{et}.

$$y = 79249x^{-0.21} \tag{2.8}$$

Then we performed a measurement of prepared bacteria solution with calculated concentration of 333 cells per milliliter. The result is shown as the thick orange curve in Fig. 2.5 (b), where R_{et} equals 25727.4 Ohm which is plotted as the green cross in Fig. 2.5 (c). According to the fitting curve, the measured concentration is 212 cells per milliliter so that the relative error is 36.4% with respect to the actual concentration. Note that this tested cell concentration is extremely low with less than one cell per microliter.

One difference between the Nyquist plot results obtained by the bench-top LCR meter and those acquired by our wireless impedance sensing platform is the shape of the curve. First, the linear part disappeared in our sensor. Because the linear part represents the diffusion-limited process and corresponds to low-frequency response. While the bench-top LCR meter can sweep

frequency starting from 1 kHz, our wireless impedance sensor starts sweeping from 2 kHz where kinetic control dominates. Second, since the upper frequency limit of the bench-top LCR meter is 1 MHz and that of our wireless sensing platform is only 100 kHz, the measurement results in the Nyquist plot converge to the origin for the bench-top equipment measurement but not for the wireless sensing platform. When we use R_{et} for calibration, because R_{et} peak for concentrations of bacteria higher than 1,000 cells/ml will fall out of the measurable frequency range, this instrument limitation shrinks the upper dynamic range to 1,000 cells/ml. As the R_{et} peak exists for a low concentration solution, the limit of detection is not degraded.

2.4 Conclusions

In summary, we have performed the design, fabrication and testing of a low-cost, miniaturized and sensitive wireless bacterial sensor that can pre-concentrate a bacteria solution to obtain a detection limit of as low as 10 cells per milliliter. In order to enable citizens to perform EIS measurement conveniently and determine whether their drinking water has been contaminated, we designed and tested a smartphone-based miniaturized impedance spectroscopic measurement platform with Bluetooth connectivity. We have used a commercial bench-top LCR meter to benchmark the performance and stability of our bacteria sensor. Additionally we integrated our sensor with the wireless impedance sensor platform to conduct a natural water sample testing after calibration. The limit of detection for the bacteria sensing is 10 E. Coli cells per milliliter and its dynamic range is from 10 E. Coli cells/ml to 1,000 cells/ml. We compared the measured E. Coli concentration with the actual cell concentration, and got the result on the same order of magnitude with an error of 36.4%. Finally, we have also proved that our Android app in the smartphone worked properly with our low-cost wireless impedance bacteria sensing platform, which enables smartphone users to measure bacterial contamination in their daily-

used water conveniently and cost-effectively. Moreover, the same wireless sensing platform and multi-stage pre-concentration filtering sensor package can be extended for specific pathogen detection by coating antibodies on the electrodes where users can detect the concentration of each kind of bacteria with a single device after performing one test.

2.5 Figures

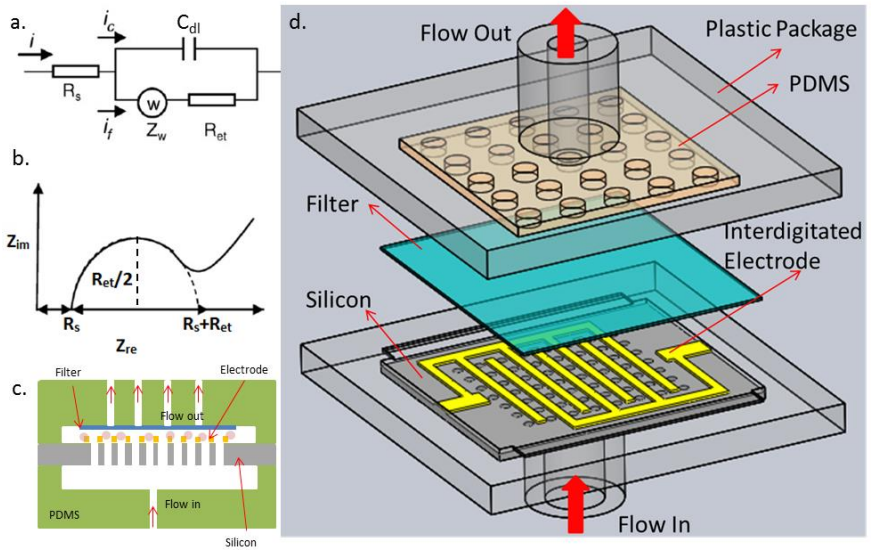

Figure 2.1 Electrochemical Impedance Spectroscopic (EIS) sensing principle. (a) Randles equivalent circuit of EIS. (b) A typical Nyquist plot for EIS. (c) Cross-sectional view of the integrated EIS bacteria sensor. (d) 3D model of the EIS bacteria sensor package.

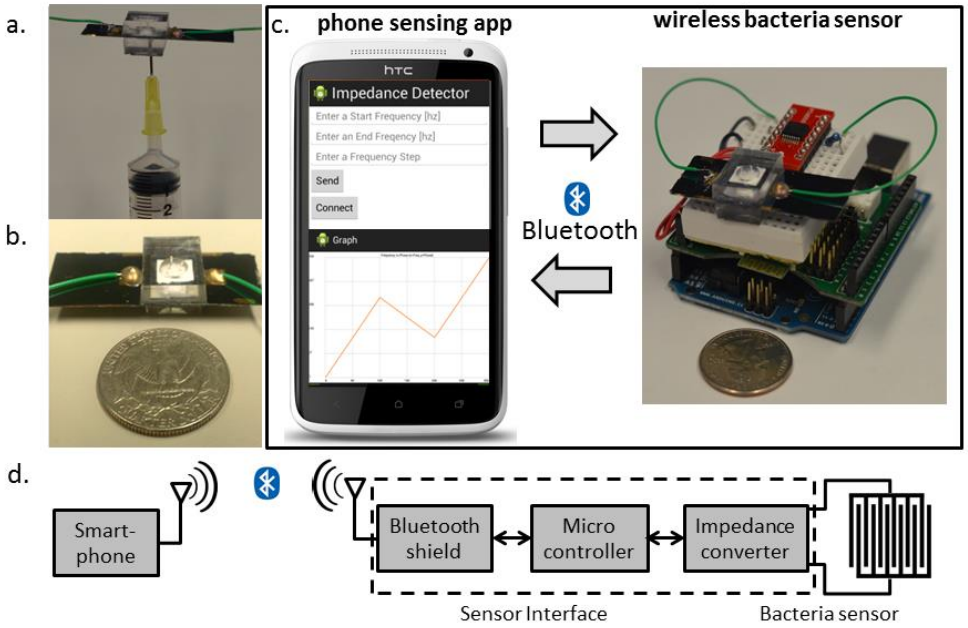

Figure 2.2 Wireless mobile phone bacteria sensing system. (a) Picture showing syringe injection of testing liquid into the sensor package. (b) Close view of the EIS bacteria sensor package. (c) Picture showing communication scheme between smartphone sensing app and wireless bacteria sensor. (d) Diagram of wireless sensing system.

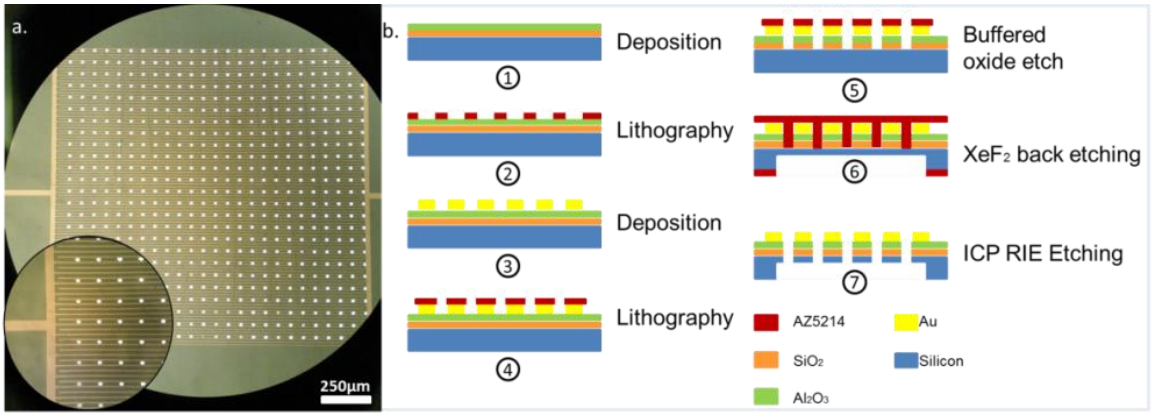

Figure 2.3 Sensor micro fabrication. (a) Top view microscopy images of the micro-hole array and interdigitated electrodes. (b) Fabrication process of the silicon sensor chip.

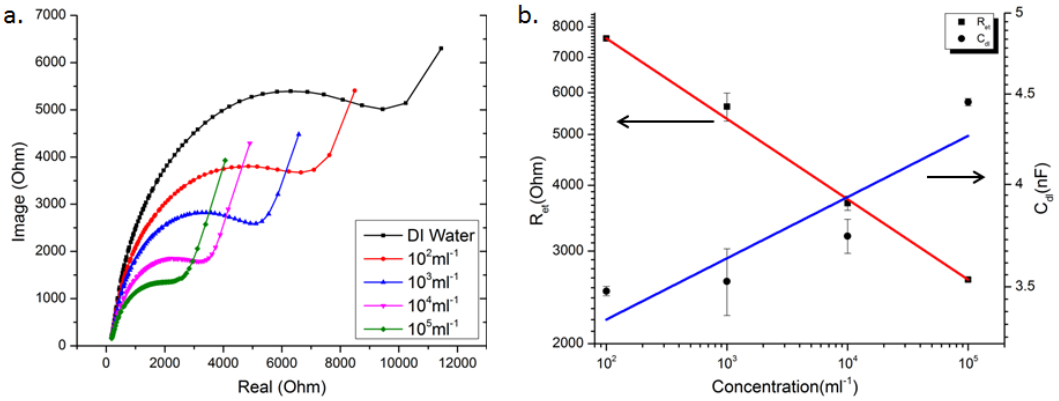

Figure 2.4 Two methods of concentration measurement using EIS bacteria sensor. (a) Nyquist plots (real and imaginary parts of the complex impedance) of bacteria solutions at different concentrations. (b) Logarithmic calibration between electron transfer resistance (R_{et}) and concentration and fitting curve (red line) and logarithmic calibration and fitting curve between double-layer capacitance (C_{dl}) and concentration (blue line).

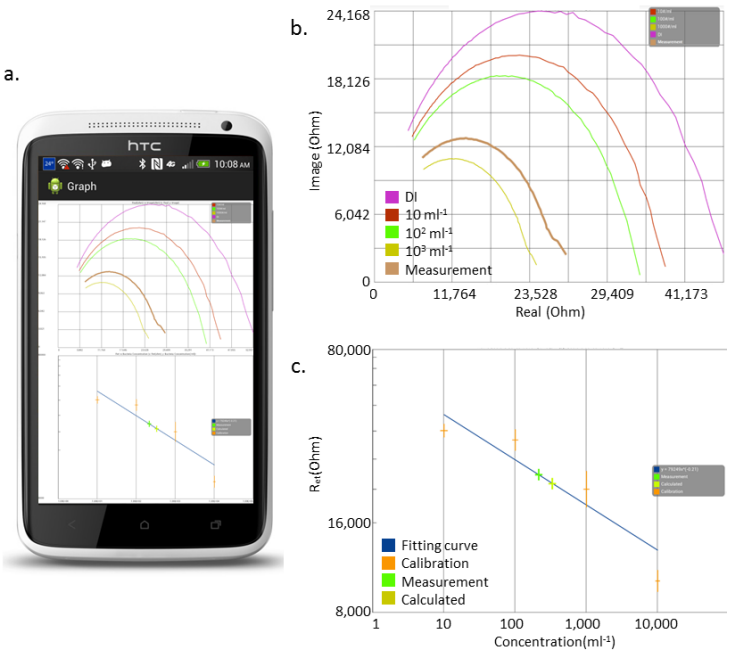

Figure 2.5 Calibration and sample measurement by the wireless cellphone bacteria sensing system. (a) Cellphone display of the impedance measurement results. (b) Zoomed-in image of Nyquist plots on the cellphone, with four solutions of known bacteria concentrations used for sensor calibration, DI water and one sample solution to be tested. (c) R_{et} vs. concentration plot and the fitted calibration curve. The E. Coli concentration of the unknown sample was derived from fitting the measurement results into the calibration curve and corresponding formula, as the green cross shows; while the yellow shows the calculated (actual) concentration and corresponding R_{et}.

CHAPTER 3: INTEGRATED PAPER-BASED BACTERIA SENSOR

3.1. Introduction

Bacteria detection is increasingly important nowadays. People are wondering whether leftover food is still edible, if the purified water they bought is really clean, if the supplied water especially in rural regions meets the safety standard. If the water or food resources that do not meet hygiene standards may contain a high population of bacteria where a portion is pathogenic bacteria. Thousands of foodborne pathogenic bacteria have been found to cause more than hundreds of known diseases, resulting 250 deaths per year in the United States.[35] Escherichia coli (E. Coli), Samonella, Campylobacter, Losteria monocytogenes, and Bacillus cereus are the major foodborne pathogen bacteria which are responsible for many foodborne illness outbreaks.[36–39] Therefore, it is very important to develop pathogenic bacteria detection methods to understand the total number of bacteria and the number of some certain species of bacteria. Meanwhile, the population of bacteria that human metabolite contains can also signify that a certain degree of phlegmonosis or infection is occurring. The ability of detecting bacteria directly in urine is also of great interest because it can save up to 5~7 days for culture and colony counting methods used traditionally and widely in hospital.[40] Understanding the result early is important for giving patients suitable and time-efficient treatment.

Current methods for bacteria determination and detection, including culture and colony counting, immunology-based methods, and polymerase chain reaction (PCR) have their own limitations. Conventional methods almost exclusively focus on microbiological culturing and isolation of the pathogen, followed by confirmation by serological tests, which takes up to 7 days to get a

confirmed result for a particular pathogenic.[40,41] Although it is reliable, it is both labor intensive and time consuming. Rapid detection methods such as enzyme linked immunosorbent assay (ELISA) and PCR have reduced the assay time to less than 24 hrs and six hours, respectively, and have achieved detection limits from 10^1 to 10^6 cfu/ml (cfu is colony forming units).[41–43]

Recently, quick detection methods for bacteria have been developed including quartz crystal microbalance (QCM), microfluidic, and the electrochemical methods.[44,45] Among modern bacteria identification and detection techniques, electrochemical impedance spectroscopy (EIS) method which can show electronic and physical properties of the detecting system has raised great interests.[46] Researchers started from using an impedance method with two bulk electrodes to detect bacteria growth in media and achieved the equivalent circuit for analyzing results.[47] Later, an interdigitated (IDT) array microelectrode has been applied for the benefits of rapid attainment of steady-state, higher signal-to-noise ratio, and the use of small sample volumes. As the improvement of a micro-fabrication technique, microfluidics has been applied to further enhance the sensitivity of bacteria detection by confining a few live bacterial cells into a small volume.[5,48,49] However, the challenges are that the height of microfluidics chamber is much higher than cells' and the detection limit is too high for a diluted sample. Dielectrophoresis (DEP) has been applied to concentrate bacterial cells from diluted samples into a very small volume.[50,51] However, it introduced additional complexities and not enough robustness on the side of the application of traditional PDMS-based microfluidics.

As one kind of new bio-sensing paradigm, the paper-based microfluidics sensing devices have been developed since 2007. Due to the low-cost and simple fabrication techniques and possibilities of application at various detection methods, paper-based microfluidics technique has been attracting attentions as a more practical microfluidics system. Methods of colorimetric sensing for detecting glucose and proteins in urine, cyclic voltammetry for detecting glucose,

lactate, and uric acid have been reported.[52–54]

Here, an integrated paper-based bacteria sensor was developed. Compared with a previous version of the bacteria pre-concentrating microfluidics sensor, this device is low cost, easy-to-use and has a very low limit of detection.

3.2 Methods and materials

3.2.1 Bacteria and filter

E. Coli samples were provided by the Institute for Genomic Biology from the UIUC with the strain number of DH5a. Water is from the MilliQ Advantage Water Purification System at the BioNanotech Lab at Micro and Nanotechnology Lab. The filter membrane is from EMD Millipore Corp., Durapore® Membrane Filter with 5 μm pore size. Electrodes are patterned by electro-beam evaporation with the Temescal six pocket E-Beam Evaporation Systems in Frederick Seitz material research laboratory at the UIUC. Flat-end copper clippers were used as connectors between the sensor and the LCR meter. An Agilent 4284a LCR meter was used for impedance measurement.

3.2.2 Paper-based bacteria sensing device

Firstly, we used Polylactic acid (PLA) plastic as the 3D printing filament to build a layer of holder (Fig. 3.1 (a)) for supporting the sensor. Secondly, two thin layers of a square array were printed separately with an Emate 3D printing filament (Shenzhen Esun Industrial Co. Ltd.) which has a low-melting temperature of 80 ^{o}C as shown in Fig. 3.1 (b). For both components, four extruded corners were printed for easy alignment. Then, Emate – sensor layer (filter with electrodes) – Emate – PLA layer are aligned and stacked together (Fig. 3.1 (c)). Thirdly, the whole construction

was baked in an oven at 90 ^{o}C for two hours. The schematic figure of the fabricated sensor is shown in Fig. 3.1 (d) where another layer of an absorbent pad is placed underneath. The saturation volume of the filter membrane is 15 μL, thus, when we inject a larger volume, this device can concentrate the solution and lower the detection limit. Figure 3.1 (e) illustrates the zoom-in picture of the sensor, showing E. Coli on the electrodes coated filter.

3.2.3 Paper-based electrode and sensor fabrication

The sensing area of the miniaturized bacteria sensor is a pair of IDT gold electrodes coated on a membrane filter. We used Epilog Mini 24 Model Laser Engraver in the Champaign-Urbana community fab lab to cut an acrylic board with the pattern of IDT electrodes to achieve the shadow mask. Then, we attached the filter of selection with the shadow mask and load it into the Temescal six-pocket E-Beam Evaporation System where we can load 12 four-inch sized samples at once. Figure 3.2 (a) shows the concept diagram of the fabrication process where gold target is bombarded by high energy electron beams in a high vacuum. Then gold atoms are evaporated to the sample. The area not blocked by the shadow mask are patterned by the gold electrodes. Figure 3.2 (c) shows the actual shadow mask we used and Fig. 3.2 (d) shows a sensor array with 20 sensors on one piece of a filter membrane after gold deposition. Figure 3.2 (b) is the image of the sensor under a scanning electron microscopy (SEM) where the left half is coated with gold, and the right half is the original PVDF filter. It can be observed that the filter structure is retained after the gold deposition.

This fabrication process is a low-cost, one-step process. The preparation of the shadow mask is quite affordable. We can prepare 12 pieces of a four-inch shadow mask in 15 minutes and the shape of the electrode can be adjusted easily and quickly. In addition, this process does not require photoresist and photolithography. On one side, it reduces the fabrication cost, on

another side, it is difficult to fully develop the photoresist at the dissolvable area where photoresist is immersed with the fiber structure.

3.3 Result

3.3.1 Concentration measurement and Hook effect

Here we measured the concentration of E. Coli which is a common bacteria and its O157 strain is so pathogenic that a few can be lethal. E. Coli samples were provided by the Institute for Genomic Biology with the strain number of DH5a to work in a Biosafety level (BSL) one environment. The E. Coli stock solution was centrifuged and rinsed with deionized (DI) water twice and diluted by 10, 100, 1000, 10,000, and 100,000 times respectively. The E. Coli concentration for the original stock solution is 107 ml-1 measured by a hemocytometer.

A 50 µL of each prepared E. Coli solution and DI water was dropped into our device in the order of increasing concentration. To test the performance of packaged sensor electronics, a commercial LCR meter, Agilent 4284A, was used as the benchmark to measure the bacteria impedance by sweeping the signal frequency from 1 kHz to 1 MHz at 1.1 times incremental frequency.

Figure 3.3 (a) shows the Nyquist plot of the results of bacteria impedance measurement. At low frequency the bacteria sensing is mass transfer controlled, while at high frequency the bacteria sensing is kinetics controlled.[31,55] In the kinetics controlled region, the diameter of the semicircle on the Nyquist plot indicates the electron transfer resistance R_{ct} according to the literature.[4,31,56] In our measurement, we observed that at low concentration less than 4M cells per milliliter, the radius of the semicircle increases as the concentration of the E. Coli increases. After extracting

the highest point of the measurement of each concentration in Fig. 3.3 (a) we have Fig. 3.3 (b) and we can see at low concentration, represented by blue dots, the impedance value increases linearly as concentration increases at a semi-log scale. The fitting formula is:

$$y = 2529.6 \ln(x) + 57304 \quad (3.1)$$

where the R^2 value is 0.9965 showing good linearity. However, when bacteria concentration is higher, this linear relationship no longer holds. If we extend the fitting curve to cover higher concentration, a high error rate was produced between the fitting curve and the measurement data. The fact that we have smaller readings at a high concentration is called the "Hook effect" or "high-dose Hook effect" in literature.[57,58] Hook effect means that the response of bio-sensor assays may give a false negative result with certain immunoassays due to a very high concentration of a particular analyze. It also happens in electrical bio-impedance measurement.[57] The following section will analyze this phenomenon and find a solution when the Hook effect occurs.

3.3.2 Circuit modeling of paper-based impedance sensor at low concentration

Traditionally, researchers used Randles model equivalent circuit for many electrochemical impedance biosensor as shown in Fig. 3.3 (a) where R_Ω is the ohmic resistance of electrolyte, C_d is double-layer capacitance, R_{ct} is the charge transfer resistance, and Z_w is Warburg impedance. Z_w has been modeled for the diffusion phenomena at low frequency showing a linear curve at a 45^o angle in the Nyquist plot.[4]

To study whether the Randles model (Fig. 3.3 (a)) works well with the paper-based impedance sensor, since our measurement data in Fig. 3.3 (a) shows a limited measurement result of the linear region in the low-frequency impedance which is controlled by diffusion, we selected another filter, Nitrocellulose (NC) membrane, whose impedance spectroscopy shows both regions of the linear part and semi-circle part, to study the equivalent circuit model, shown as red dots in Fig. 3.3 (b). The fitting result (in green) shows that at high frequency or the semi-circle region, the Randles model has a good fitting with the measurement data; while at low frequency or the linear region, the measurement dataset is curved while the calculated data is a straight line.

After studying the possible differences between the Randles model and our experiment condition and running different equivalent circuit models to fit the testing data, we designed an improved equivalent circuit model shown in Fig. 3.3 (c), where Z_w is replaced by a QR loop and C_d is replaced by Q_d. Q is called a constant phase element (CPE), defined by

$$Q = \frac{1}{Q_0 \omega i^n} = \frac{1}{Q_0 \omega^n} e^{-\frac{\pi}{2} n i} \tag{3.2}$$

where Q_0 and n ($0 < n < 1$) are frequency independent, ω is frequency. Q_0 equals the magnitude of its admittance at

$$\omega = 1 \text{ rad/s} \tag{3.3}$$

Q is used to model the behavior of a capacitor with imperfect dielectrics within it. n signifies the quality of the capacitor. The case n = 1 describes an ideal capacitor while the case n = 0 describes a pure resistor.[59]

From the fact that we achieved much better fitting shown in Fig. 3.3 (d) especially at the low-frequency region with the improved model, we know this model is a success. The reason why we made these two changes are, (1) the double-layer capacitor has been replaced by CPE from a capacitor for the double-layer effect because the double-layer capacitance is actually a "leaky" capacitor. By replacing the circuit model into a CPE, we achieved slightly better fitting at the semi-circle region, since the "n" we extracted from the fitting model was between 0.949 and 0.977, very close to 1. (2) The Warburg impedance was replaced by a QR loop, because the Warburg impedance correctly models the diffusion process from a planar electrode; here from Fig. 3.2 (b) we can see, the e-beam evaporated electrodes on filter membrane has many nano-size spheres as the electrode so that Warburg impedance is not applicable in our case. According to Fig. 4.14 (a) in the book edited by A. Lasia,[60] as the radius of electrodes becomes smaller, the impedance in a Nyquist plot is close to ellipse shape. To represent this characteristic better, in the improved model we replaced the Warburg impedance to a QR loop which gives an ellipse shape on Nyquist plot.

With this improved model (shown again in Fig. 3.4 (a)), we can successfully fit four curves from DI to 400 cells per milliliter in Fig. 3.4 (b). When we extract the R_{ct} from the fitting parameter and plot it according to the concentration, we have a linear relationship in a semi-log scale, the formula is:

$$y = 4785.9 \ln(x) + 128085 \tag{3.4}$$

the R^2 is 0.9992. Here, ideally we expected to have R_{ct} to be twice of R_{peak}. From the comparison, roughly we can observe for the result we expect.

3.3.3 Circuit modeling of paper-based sensor at high concentration

From previous studies, we can successfully fit the data at low concentration with the improved model in Fig. 3.4 (a). However, when we tried to fit the measurement data at a higher concentration with that model, we could not achieve a good fit, shown in Fig. 3.4 (d). Moreover, in Fig. 3.4 (i), the trend of height of the semi-circle region decreases when the concentration is larger than or equal to 4M cells per milliliter. We do not believe the improved model is still applicable at high concentration. We will build a good model for the case with a high concentration of bacteria.

The fact that the impedance decreases when the bacteria concentration increases reminded us about pearl chain effect in the literature.[31,36,48,61] When the alternating current (AC) electrical field is applied, cells have the tendency to form lines due to the dielectrophoresis effect. When we performed the experiment on a piece of glass slide coated with IDT electrodes and took a video of the sensor while AC excitation signal was being applied, we could clearly see that cells form lines at high concentration as shown in Fig. 3.4 (e). When bacteria form chains across the pairs of electrodes, the overall impedance decreases because each chain can be modeled as a resistor and a capacitor connected in parallel, as shown in Fig. 3.4 (f).[61] The proposed equivalent circuit model for the high concentration case is in Fig. 3.4 (g) where a parallel connected $R_{pc}C_{pc}$ (pc means pearl chain) is added to the improved model. A very good agreement has been reached between the simulation and measurement at both 40M and 400M cells per milliliter. When we extracted the R_{pc} from the fitting parameters, and plotted them with respect to the concentration of bacteria, we have Fig. 3.4 (h) from which we can observe that when the concentration of bacteria increases, the R_{pc} decreases because more chains are formed equivalent as more resistors connected in parallel; with more resistors in parallel, overall R_{pc} is smaller.

3.4 Conclusion

In this study, we have developed a paper-based impedance bacteria sensor that can detect E. Coli concentration as low as 400/ml. The cost per unit is only 60 cents based on the facility charge of MRL at the UIUC and filter membrane cost. We also observed and explained the Hook effect and use this to significantly lower our sensitivity. Besides, the dynamic range is from 400 cfu/ml to 4 Mcfu/ml. As long as the target concentration is in this range, we can easily measure the bacteria concentration with our sensor. For samples of high concentrations, the solution will appear milky. Thus, this detection method is not necessary since users can identify the pollution by eye.

3.5 Figures

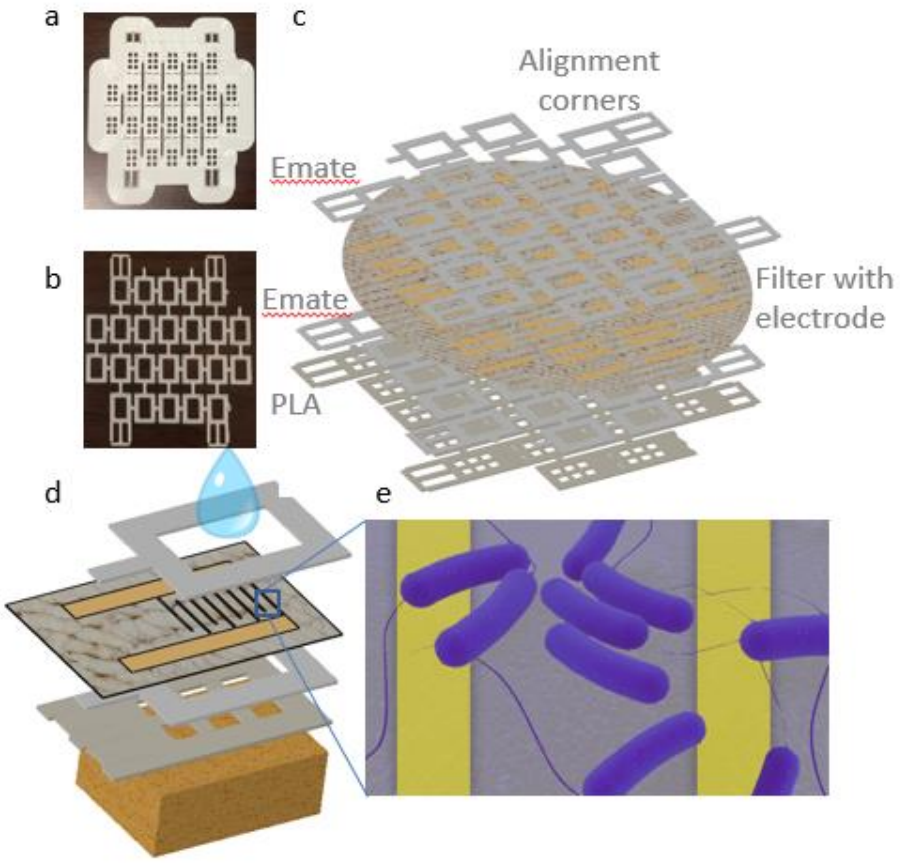

Figure 3.1 (a) 3D printed PLA supporting layer. (b) 3D printed Emate frame for confining the liquid sample. (c) The schematic graph showing the stacking configuration of Emate-filter-Emate-PLA, which will be aligned, stacked, baked. (d) The configuration of a sensor with an absorbent pad underneath. (e) The illustration of a zoom-in picture of the sensor, showing E. Coli on the electrodes coated filter.

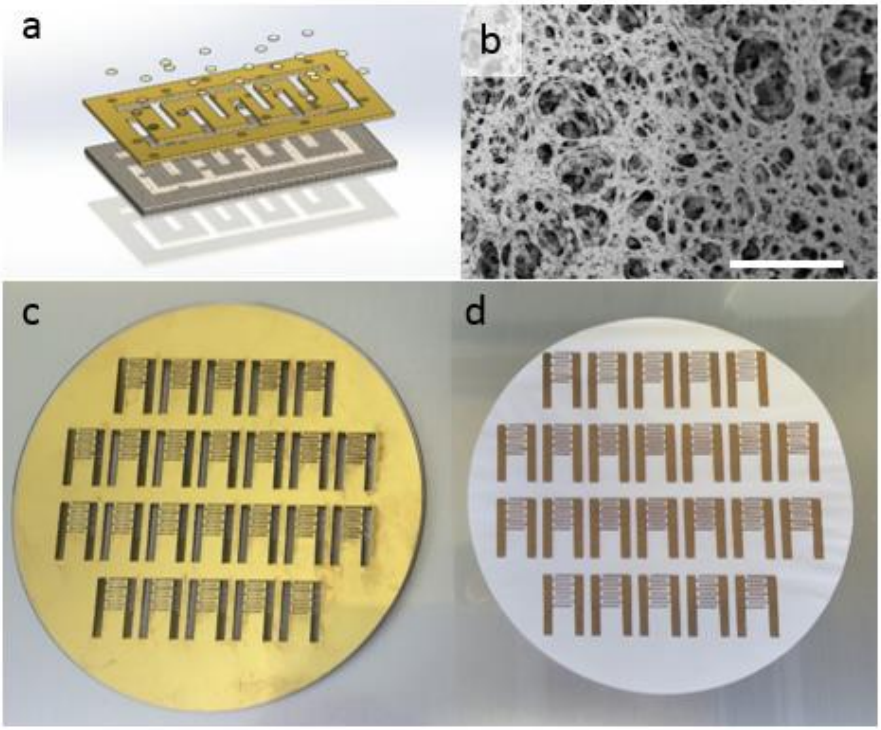

Figure 3.2 (a) Illustration of e-beam evaporation process with a shadow mask: the top layer is the shadow mask, the bottom layer is the filter. (b) SEM picture of the PVDF filter membrane. Left half is coated with gold, right half is uncoated. (c) Transparent acrylic shadow mask after gold deposition. (d) Filter membrane after gold deposition.

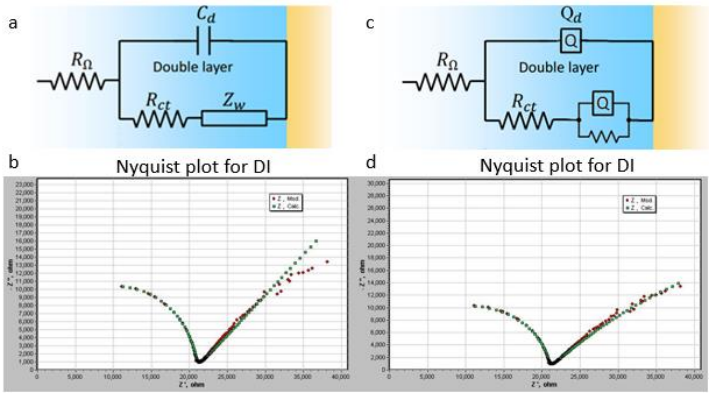

Figure 3.3 (a) Traditional Randles model. (b) Measurement data (red) and fitted data (green) with Randles model of impedance of DI water on NC membrane. (c) Improved model for paper-based impedance measurement. (d) Measurement data (red) and fitted data (green) with our new model of impedance of DI water on NC membrane.

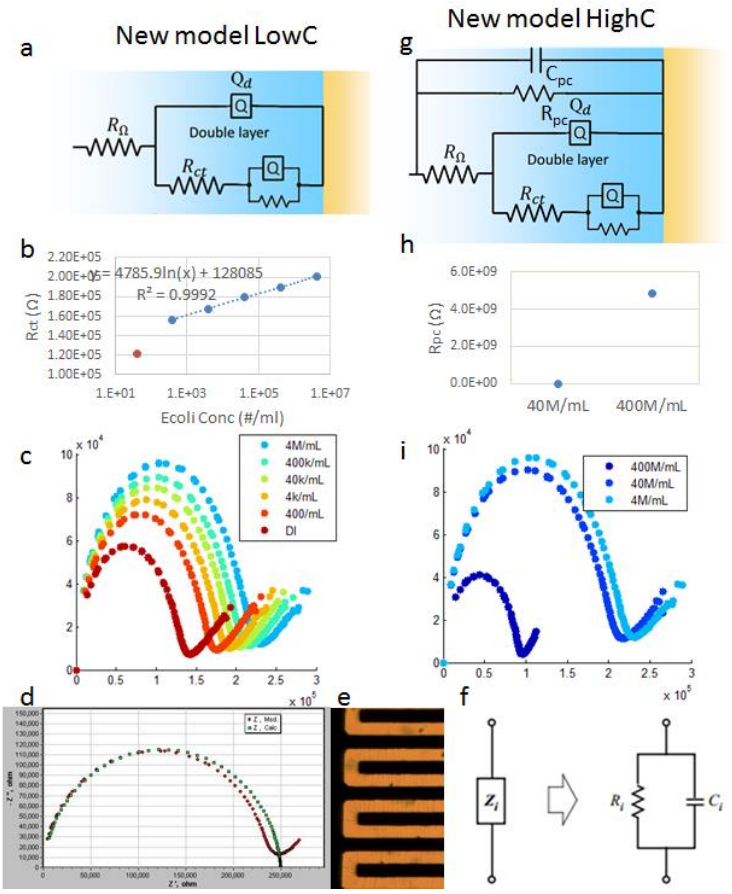

Figure 3.4 (a) The new model, only effective to measure bacteria at low concentration. (b) Extracted charge transfer resistance for low-concentrated bacteria measurement and the fitting curve. (c) The Nyquist plot of measurement data for bacteria at low concentration. (d) Fitting (green) the measured data (red) at high concentration with our “new model”. (e) Microscopic image of bacteria impedance measurement, lines (pearl chain) are formed. (f) Equivalent circuit model for bacteria in pearl chain. (g) Modified new model to evaluate bacteria at high concentration. (h) Extracted pearl resistance for high-concentrated bacteria measurement and the fitting curve. (i) The Nyquist plot of measurement data for bacteria at high concentration (40 M/ml and 400 M/ml).

CHAPTER 4: SECOND REPLICATED 3D PLAMONIC SILVER SERS SENSOR

4.1 Introduction

The increasing demands of medical diagnostics, environmental monitoring, drug screening and food safety control entrust the development of highly selective, sensitive and low-cost sensors with foremost importance. Among the various sensors, optical sensors based on plasmonics are becoming the method of choice in label-free analysis of biomolecular interactions. Recently, due to the advancement of nanofabrication technology, noble metallic nano-structures with unique plasmonic properties like surface plasmon resonance (SPR) and localized surface plasmon resonance (LSPR) reveal their advantages in different applications such as chemical and biological sensing, subwavelength imaging and energy harvesting.[62–64] The principle of the SPR or LSPR sensors is mostly based on measuring the shift of plasmonic resonance peak wavelength induced by the refractive index (RI) change of the environment.[65] For higher sensitivity of RI sensing, larger absolute wavelength shift of resonance peak per unit RI change and higher quality-factor (height to width ratio) of the resonance peak are desired. But there is usually a trade-off between the two desired properties. Taking the two most commonly used schemes - subwavelength grating structure and colloidal metallic nanoparticles, for example, the subwavelength grating structure with a Kretschmann configuration has been proved for its ultrahigh sensitivity (~10^6 nm/RIU) with a high quality-factor, but the absolute wavelength shift is only a few nanometers.[66] Such a small wavelength shift requires a sophisticated spectrometer for detection. On the other hand, LSPR sensing based on colloidal metallicnanoparticles has a much larger wavelength shift which requires less equipment, making naked-eye plasmonic colorimetry possible.[67] However, the colloidal metallic nanoparticles sensing has lower accuracy due to its lower quality-factor, less

uniformity and worse reproducibility. These performances are mainly caused by the factors which can affect the LSPR dramatically while difficult to be controlled precisely, such as particle size, shape and distribution.[68] Plasmonic sensors for RI sensing are very good for label-free quantitative analysis but not good for qualitative analysis. In contrast, Raman spectroscopy is very good at qualitative identification and analysis with the distinctive vibrational features of molecules. However, the cross section of Raman scattering is so small (1 in 10 million) that highly sensitive spectrometer or highly concentrated target analysis is required. Fortunately, surface-enhanced Raman spectroscopy (SERS) can significantly enhance the Raman scattering by an order of 10^6 to 10^{10} thus greatly improve the sensitivity of Raman spectroscopy, even making the detection of a single molecule possible.[69] However, SERS, which relies on the specialized noble metallic nano-structures, has its own limitations such as low repeatability, non-uniformity, high cost, complicated fabrication process, low throughput and small area. These drawbacks thwart the wide application of SERS. Especially, the low uniformity and small area hamper the quantitative analysis by SERS.[70] To date, there has been a lot of work reported on either SERS or plasmonic sensing but very few have reported sensing with the same device for both SERS and plasmonics, let alone plasmonic colorimetry sensing by naked eye. Sensing based on the shift of plasmonic resonance peak is very sensitive with the detection of RI change, thus it is good at quantitative analysis. On the other hand, SERS is very sensitive at the qualitative detection of chemicals by their distinct Raman spectra while not very well at quantitative analysis. The unsuitability of SERS for quantitative analysis is mostly attributed to low reproducibility, non-uniformity and the small area of SERS substrates.[71–73] Nanohole-array structure has been demonstrated for both plasmonic colorimetric RI sensing by naked eye[74,75] and SERS.[76,77] The nano-pillar or nano-cone structure has been designed with different techniques for plasmonics application, colorimetric sensing and Raman scattering enhancement. For example, a periodic nano-pillar structure was fabricated with electron-beam (e-beam) lithography,[78] focused ion

beam (FIB) milling,[79] and laser interference lithography.[80] Some of them have good Raman scattering enhancement and others demonstrate color change with the periodicity of the nano-structure. However, all of them are limited by low throughput and high cost. The nano-imprint technique with lower cost produced low yield of the nano-pillar substrate.[81] Other low-cost methods such as nano-sphere lithography use polystyrene nano-spheres as etching masks to produce semi-periodic nano-pillars.[82] The anodized aluminum oxide (AAO) technique uses porous AAO as a template to form a metal nano-pillar[83] or form polymeric nano-pillar after nano-imprint.[84] Even though those nano-pillar or nano-cone structures are widely used for SERS, none of them demonstrated colorimetry by using the naked eye.

In this chapter, we demonstrated a dual-mode plasmonic colorimetry and SERS substrate based on plastics. Due to its plastic nature, we named this substrate FlexBrite because it is bendable. Figure 4.1 (a) is a photograph of a piece of FlexBrite. The large-area uniformity of this dual-mode sensor makes quantitative Raman analysis and colorimetric RI sensing possible. A SEM image of the nano-structure of FlexBrite is a nano-mushroom array, shown in Fig. 4.1 (b). The special nano-mushroom structure differentiates it from the ordinary nano-cone or nano-pillar structure and has special properties for both plasmonic colorimetry and SERS. As shown in Fig. 4.1 (a), FlexBrite shows a purple color without any liquid on the surface from a rough top-view perspective. If the perspective angle becomes larger, then the purple color will gradually change to blue (45^o ~ 60^o), green (60^o ~ 75^o) and red (75^o ~ 90^o). All the colorimetric sensing images were taken with a rough top-view perspective. Figure 4.1 (c, d) roughly demonstrate the colorimetric property of FlexBrite. Figure 4.1 (c) demonstrates a water droplet stays on the surface of substrate showing green while the FlexBrite substrate itself looks purple. Figure 4.1 (d) shows that different liquids with difference RI will present different colors on FlexBrite. Water (n = 1.333) looks green while cedar wood oil (n = 1.518) looks red on the surface of FlexBrite. Compared to our previous work of

naked-eye colorimetry by using a Lycurgus nano-cup array structure (nanoLCA), the colorimetric properties of FlexBrite has two major advantages. One advantage is FlexBrite works better in a reflection mode, which makes the measurement easier and more accurate. The colorimetry of NanoLCA sensor works in transmission mode, in which the detector must be placed on the other side of sample liquid. In the transmission mode, the detector and light source are separated on two sides of the sample, so the transmitted light was dimmed by the sample. The plastic substrate and especially the metal layer with a thickness of 80 nm to 90 nm, will lower the accuracy of the measurement. Also for this reason, the backside of nanoLCA sensor has to be kept very clean. FlexBrite works in the reflection mode, in which the light source and detector are on the same side of the sample so FlexBrite does not have the problems of dimming and backside cleaning. The other advantage is that FlexBrite has a wider color range and higher sensitivity for colorimetry. For air, water and oil, respectively, nanoLCA shows green, yellow and red color while FlexBrite shows purple, green and yellow/red, which covers a larger spectra range. In addition to colorimetry, FlexBrite has a SERS property with the enhancement factor of 10^8 and large-area uniformity with small variation of within 15%. We also found that the SERS of FlexBrite excited by a 633 nm laser is seven times stronger in a wet state than in a dry state, making FlexBrite suitable for an aqueous environment such as microfluids. The seven times enhancement in a wet state was explained by both the finite-difference time-domain (FDTD) simulation and reflection measurement. We demonstrated two applications of FlexBrite. One is detection of the biotin-streptavidin interaction by both SERS and colorimetry while the other is detection of a trace amount of the narcotic drug methamphetamine in drinking water by SERS with a handheld Raman spectrometer and FlexBrite.

4.2 Result and discussion

4.2.1 Characterization of colorimetry of FlexBrite

In Fig. 4.1 (c, d) we have roughly demonstrated the colorimetric property of FlexBrite. For a quantitative analysis of colorimetry, we prepared glycerol solutions with different concentrations for different RI. The RI of glycerol solutions with different concentrations at room temperature were looked up in a table provided by Dow Chemical. The liquid was dropped on the surface of FlexBrite then covered with a coverslip. Figure 4.2 (a) is a series of images of FlexBrite with the liquid of different RI. These images were taken in a reflection mode with an Olympus BX51 upright fluorescence microscope equipped with a 20X objective lens, DP50 digital camera and a mercury lamp. We kept the same camera setting for all the images. Exposure time of 30 ms. RGB gain was set to 1. As the RI of liquid increases from 1.333 (water) to glycerol solutions with different concentrations (RI from 1.357 to 1.474) then to 1.518 (cedar wood oil), the color of FlexBrite changes from green to yellow and then to red. Then we can say that the color of FlexBrite is red-shifted as the RI of liquid increases. Figure 4.2 (b, c) show the averaged RGB and HSV values of the images in Fig. 4.2 (a). From Fig. 4.2 (b), we can see the red (R) channel increases while the green (G) and blue (B) decrease as the RI of liquid increases, which matches the red-shift trend observed by naked eye in Fig. 4.2 (a). The R and G channels almost follow a linear relationship with RI. From Fig. 4.2 (c), we can see the saturation (S) increases while hue (H) decreases with RI increases but value (V) does not follow a clear trend with RI. As a result, we can use R, G, B or S, H to quantitatively measure the RI of liquid on the surface of FlexBrite. Considering R and G have better linearity, we prefer to use R and G as the indicators of the RI of liquid. To prove the reusability of FlexBrite colorimetry, we alternatively replaced the liquid in the microfluidic channel with water and glycerol solutions and recorded the process. Figure 4.3 (a) is a series of

video snapshots. As we replaced the liquid alternatively with water and glycerol then water again, the color FlexBrite turned from green to red then to green again. We can see the RGB and HSV values also alternatively change with time. Taking the R value in Fig. 4.3 (b) for example, it suddenly rises after water is replaced by glycerol, corresponding to green turning to red in Fig. 4.3 (a). Then the R value drops back to its previous value after glycerol is replaced with water, corresponding to red turning back to green in Fig. 4.3 (a).

In addition to the image RGB and HSV analysis of colorimetry of FlexBrite, we also used spectroscopy to characterize the colorimetric property of FlexBrite. Figure 4.4 (a) shows the reflection spectra from liquids with different RI on its surface. The reflection spectra were taken with the same Olympus BX51 upright microscope and Ocean Optics USB2000+ Fiber Optic Spectrometer. We can see the peaks of reflection spectra were shifted to longer wavelength as the liquid RI increases, corresponding to the red-shift we observed in the images in Fig. 4.2(a). We plotted the peak wavelengths in Fig. 4.4 (a) versus the liquid RI in Fig. 4.4 (c). We calculated the slope of linear regression of the data in Fig. 4.4 (c) to get the sensitivity of 611 nm/RIU. FlexBrite's high RI sensitivity of 611 nm/RIU enabled naked-eye detection.

4.2.2 FDTD simulation

To investigate the mechanism of FlexBrite's high sensitivity in colorimetry and predict the optimal structure of the nano-mushroom, we use the finite-difference time-domain (FDTD) method to simulate the reflectance spectra according to its nano-structure. Looking at the nano-structure of FlexBrite as shown in the SEM images in Fig. 4.1 (b) and Fig. 4.5 (a), we propose that the high sensitivity for colorimetry is due to the combination of surface plasmonic resonance (SPR) of the periodic structures of the nano-mushroom array and localized surface plasmonic resonance (LSPR) of the silver nanoparticles on the sidewall of the nano-mushroom. Considering the complexity of

the nano-structures of FlexBrite, the simulation is not trivial. To mimic the nano-mushroom structure, we create a model with several variable geometric parameters, shown in Fig. 4.5 (b), to resemble the real structure of the nano-mushroom (Fig. 4.5 (a)). The variable geometric parameters of the nano-mushroom include the diameter d_1 of the sphere on the top, the diameter d_2 of the small spheres on the sidewalls, the conic angle θ of the polymer nano-pillar, and the thickness t of the silver layer on the flat surface. From the SEM images of the nano-mushroom, we can see there are a lot of particulate silver particles on the sidewalls of nano-mushrooms. We modeled the silver particles as small spheres on the nano-mushroom sidewalls. To match the measured reflection peaks with the simulated reflection peaks at different liquid RI, the method of particle swarm optimization was used to find the optimal geometric parameters which allow the simulated peaks to be matched with measured peaks. Due to some irregularities of the real nano-structures as we can see in the SEM images in Fig. 4.1 (b) and Fig. 4.5 (a), for the same FDTD model, it is impossible to get exactly the same peaks for simulation and measurement at different RI values of the liquid. In the optimization process, we tried to minimize the difference between the simulated peaks and measured peaks all added together. Figure 4.5 (c-e) are some tentative geometries during the optimization with Fig. 4.5 (e) as the optimal geometry we finally got. Figure 4.4 (b) is the simulated reflection spectra after optimization. The simulated peaks were plotted in Fig. 4.4 (c) to compare with measured peaks. The peaks of reflection spectra in Fig. 4.4 (b) match very well with the measured peaks in Fig. 4.4 (a).

4.2.3 SERS characterization

To characterize FlexBrite on its surface-enhanced Raman spectroscopy (SERS) properties, we used 1,2-bis(4-pyridyl)ethylene (BPE) which will form a uniform monolayer on the silver surface after surface functionalization. For functionalization with BPE, FlexBrite was immersed in 100 μM BPE

ethanolic solution for five hours and then rinsed in pure ethanol, followed by blow drying with nitrogen to ensure a uniform single molecular layer adsorbed on the surfaces,[85] in which the BPE functionalization time is 24 hours. However, previously in a kinetic study of SERS intensity versus functionalization time, we found the minimum functionalization time for stable and reliable SERS intensity is five hours. For Raman spectroscopy, we used the Renishaw Raman spectrometer with 20X objective lens and a He-Ne laser with 633 nm wavelength for excitation. The Raman enhancement factor (EF) was calculated by comparing the SERS signal intensity of BPE on FlexBrite with the BPE bulk solution. The EF of FlexBrite in a dry state (no liquid on its surface) was calculated as 6.85×10^7. To verify our calculation of the EF of FlexBrite, we used the commercial Klarite SERS substrate which is claimed to have the EF of 10^6. We treated the Klarite substrate the same way as we treated FlexBrite with BPE incubation and measured the Raman signal. Figure 4.6 (a) shows the SERS comparison of FlexBrite with Klarite. With the same laser power and integration time for excitation, we found the SERS signal of FlexBrite is 60 to 80 times stronger than Klarite. For visual reasons, we used a higher excitation power of 1.23 mW for Klarite SERS and smooth silver while lower excitation power of 211 μW for FlexBrite SERS and plotted them on the same graph as shown in Fig. 4.6 (a) for comparison. To characterize the uniformity of the SERS of FlexBrite, we used the mapping function of the Renishaw Raman spectrometer, that is, a spatial 2D array of single Raman measurements at each point in the array. Figure 4.6 (b-d) show the result of SERS uniformity testing of FlexBrite with a 21 × 21 array with the period spacing of 0.5 mm for mapping. Figure 4.6 (b) is a series of SERS spectra of BPE at different locations in the mapping array. Figure 4.6 (c) is the averaged SERS spectra of all the measurements in the mapping array, with the cyan shadow as the standard deviation. In Fig. 4.6 (d), the peak intensity at the wavenumber of 1607 cm^{-1} was used to plot the distribution of SERS enhancement for the mapping array on FlexBrite. The variation of SERS intensity is below 15% for the area of 10 mm × 10 mm.

The previous measurement was done in a dry state (no liquid on the surface). Considering the FlexBrite will present color change with liquid of different RI on the surface, we are interested in the SERS of FlexBrite with liquid on the surface, or wet state. Shown in Fig. 4.6 (e), water was dropped on the surface of FlexBrite after BPE incubation for five hours at a wet state. From the top view, FlexBrite became green with water due to its colorimetric property. Then the 633 nm laser was shined and focused on the surface of FlexBrite for spectrum acquisition. With the same configuration we used for measurement in the dry state, we found that the SERS signal of BPE for the wet state FlexBrite is about seven times stronger than SERS in the dry state. Figure 4.6 (f) shows the comparison of dry state (RI = 1) SERS and wet state (RI = 1.333) SERS of FlexBrite. To investigate the phenomenon that wet-state SERS of FlexBrite is much stronger than dry-state SERS, we compared both the measurement and FDTD simulation of the reflection spectra of FlexBrite in dry and wet states, shown as Fig. 4.7 (a). The solid curves in Fig. 4.7 (a) are the measured reflection spectra for dry state (blue) and wet state (red), while the dashed curves in Fig. 4.7 (a) are the simulated reflection spectra for the dry state (blue) and wet state (red). For both measured and simulated reflection spectra, we can see a valley close to the excitation wavelength of 633 nm for the wet state while no valley was seen around 633 nm for the dry state. This indicates that the nano-mushroom structure of FlexBrite is on resonance at 633 nm in wet state. The seven times enhancement of SERS in the wet state is caused by the plasmonic resonance around the excitation wavelength of 633 nm. According to the electromagnetic theory of SERS, the SERS enhancement factor is proportional to E^4, the 4^{th} power of electric field intensity.[86] Around the metallic nano-structures, only the locations where the electric field is very strong will have the SERS effect and those locations are referred to as “hot spots”. To verify the enhancement due to resonance, from the FDTD simulation model we took the cross sections of the electric field distribution around a nano-mushroom at 633 nm in Fig. 4.7 (b). In the FDTD model, the intensity of the electric field of the incident wave is defined as unit 1. The electric field distribution in the

dry state is shown on the left and that in the wet state is shown on the right with the same color bar as the scale of the electric field intensity compared to the incident field. From Fig. 4.7 (b) we can see that there are more “hot spots” around the nano-mushroom of FlexBrite in the wet state than in the dry state. This indicates that the nano-mushroom is on a resonance of 633 nm in wet state and explains the stronger SERS of FlexBrite in the wet state.

4.2.4 Visible detection of biotin-streptavidin interaction by FlexBrite

Detection of biomolecular interaction such as antibody-antigen binding, DNA hybridization are common and critical in biochemical assays. Extensive explorations have been done for easy and fast label-free detection of biomolecule interactions using the methods such as field effect transistor (FET) sensor,[87] microcantilever sensor,[82] localized surface plasmon resonance (LSPR),[88] and whispering gallery mode microcavities.[89] In this work, to demonstrate the label-free detection of biomolecular interaction with FlexBrite by both naked-eye colorimetry and SERS, we chose biotin–streptavidin interaction as a model system because they are well-studied binding partners that interact with very high affinity and are often used for proof-of-concept for detection of biomolecular interaction.[90,91] We used the thiolated biotin to form a uniform monolayer on the silver surface of FlexBrite after 24 hours of incubation. The biotin-streptavidin functionalization was done by incubating the FlexBrite with biotin in a streptavidin solution for two hours then rinsed with ethanol. Figure 4.8 (a) shows the schematic of biotin functionalization and biotin-streptavidin binding on the surface of FlexBrite. Prior to the measurement with colorimetry and SERS, we dropped water on the surface of FlexBrite just like how we characterized the FlexBrite in the wet state. We measured the reflection images, spectra and SERS before and after the biotin functionalization and biotin-streptavidin binding respectively. Figure 4.8 (b) shows the colorimetric images of FlexBrite in water with a biotin monolayer and after biotin-streptavidin

binding. We can see that after formation of the biotin monolayer, the color of FlexBrite changed a lot from green to yellowish green. After biotin-streptavidin binding, the color changed a little toward the red, close to yellow. Figure 4.8 (c, d) show the averaged RGB and HSV values for FlexBrite in water, with biotin and after biotin-streptavidin binding. The R value shows a clear trend of increasing after each step, indicating a red-shift, shown in Fig. 4.8 (e). From the reflection spectra in Fig. 4.9 (a), we can see the red-shift of the reflection peak after each step. The reflection peak was shifted from 508 nm in water to 548 nm for the biotin monolayer then to 575 nm after biotin-streptavidin binding. In addition to colorimetry, SERS was also used to investigate the biotin-streptavidin binding. In Fig. 4.9 (b), the SERS spectra of biotin-monolayer on FlexBrite were compared before and after binding with streptavidin. After biotin-streptavidin binding, the intensity of SERS was lower and showed fewer peaks. The modification of the SERS spectrum implies a change in the secondary structure of the host biomolecule biotin. For example, the much less intense peak at 1287 cm^{-1} in the presence of streptavidin implies the decrease of the amount of the β-sheet conformation.[92] SERS is a near-field effect which decreases 10 to 12 fold with the distance from the analyte to the metal surface.[93] The weaker overall SERS signal after streptavidin binding may be due to the coverage of the 52.8 kDa protein streptavidin which blocks the SERS signal from the nano-mushroom.

4.2.5 SERS detection of narcotic drug with handheld spectrometer

The low cross-section of Raman scattering requires either a highly concentrated sample or a highly sensitive Raman spectrometer to get a detectable signal. For this reason, the low-cost and convenient handheld Raman spectrometers are mostly used to identify highly concentrated samples such as minerals due to their relatively lower sensitivity.[94] If the sensitivity of a handheld Raman spectrometer can be greatly enhanced by SERS, then the fast and easy detection of a trace

amount of most organic chemicals can be implemented. To demonstrate that the sensitivity of a handheld Raman spectrometer can be boosted by FlexBrite, we used the SERS property of FlexBrite to detect the narcotic drug methamphetamine in drinking water with a handheld B&WTek NanoRam handheld Raman spectrometer. Figure 4.10 showed several snapshots for the detection of methamphetamine. A small piece of FlexBrite was cut off from the 4-inch wafer and glued onto the inner wall of a glass vial used with a NanoRam spectrometer, shown as Fig. 4.10 (d). In Fig. 4.10 (a), the methamphetamine was diluted in water with the concentration of 1 mg/L (about 1 ppm). Then the diluted 1 ppm methamphetamine solution was sent by a pipette into a vial without FlexBrite for Raman testing with the NanoRam spectrometer. The test result of the vial without FlexBrite was shown in Fig. 4.10 (c), in which no Raman peaks of methamphetamine was seen. The big hump of the spectrum is from the autofluorescence of the glass vial. Then the same 1 ppm methamphetamine solution was added into the vial with FlexBrite and tested with NanoRam spectrometer with the same configuration. Figure 4.10(d) shows that the Raman peaks of methamphetamine were detected with FlexBrite in the vial. We proved that with FlexBrite the sensitivity of the handheld Raman spectrometer can be greatly enhanced, therefore it can be used for easy and fast detection of trace amounts of chemicals.

To find the limit of detection of methamphetamine with FlexBrite, we tested methamphetamine in an aqueous solution with different concentrations, as shown in Fig. 4.10 (g). The lowest concentration of methamphetamine we could constantly detect is 0.5 mg/L. When the concentration of methamphetamine is high as 100 mg/L, the Raman signal is higher. The Raman signal does not vary too much in the concentration range of 1 mg/L to 10 mg/L. The explanation is that at high concentration much of the Raman signal comes from the bulk solution itself so the Raman intensity is related to the concentration. But at a lower concentration, the Raman signal mostly comes from SERS, which comes from molecules adsorbed on the FlexBrite surface, so the

Raman intensity does not change much with the concentration. The lowest concentration at which we can constantly detect a Raman signal is 0.5 mg/L. When the concentration gets lower than 0.5 mg/L we can get the Raman signal occasionally but not always. As a result, we claim that 0.5 mg/L is the reliable limit of detection of methamphetamine.

4.3 Experiment section

4.3.1 Fabrication process

The nano-mushroom substrate was fabricated by a nano-replication process. The original mold was a nano-cup array on a silicon oxide wafer fabricated by laser interference lithography followed by ion milling deep reactive ion etching.[80] Prior to replication, the mold was treated with silane for hydrophobicity.[95] The nano-pillar array was produced by molding the nano-cup array with Norland Optical Adhesive 61 ("NOA 61"). Then 9 nm of titanium and 90 nm of silver were deposited onto the nano-pillar array by e-beam evaporation. The titanium layer is to improve the adhesion. After the metal deposition, the nano-mushroom structure will be formed. However, to this point, the nano-mushroom surface is very hydrophobic, which will prevent the aqueous solution from contacting the surface and the adsorption of target molecules. To make the surface hydrophilic, we deposited a very thin layer of silicon oxide SiO_2 onto the nano-mushroom surface by physical vapor deposition (PVD) for five seconds. We used the K. J. Lesker PVD 75 system for the thin SiO_2 deposition. We injected argon to 1.5 mTorr after evacuated the chamber down to $3e^{-6}$ psi. Then 300 W plasma was ignited with the 3” PVD gun for the deposition at room temperature. The actual thickness of the SiO_2 layer is too thin to measure directly. But by ellipsometry we measured the deposition rate for thicker SiO_2 with a longer deposition time. The deposition rate can fluctuate. On average, the deposition rate was found to be one angstrom per second. We barely deposited for five seconds for the thin layer. As a result, the thickness of silicon

oxide is estimated to be about five angstroms.

4.3.2 Colorimetry measurement

The colorimetry measurement was taken with an Olympus BX51 upright fluorescence microscope equipped with a DP50 digital camera and a mercury lamp. We keep the same camera setting for all the images. Exposure time of 30 ms. RGB gain was set to be 1. The microscope was set at bright field mode without applying any filter. The light was focused onto the sample with a 20X (NA = 0.45) objective lens. The reflectance spectra were collected by the sample microscopy setup with USB2000+ Fiber Optic Spectrometer by Ocean Optics. The detection wavelength range is from 200 to 1100 nm and the spectral resolution is up to 0.3 nm FWHM.

4.3.3 FDTD simulation

The numerical simulations of optical characteristic were studied by using a three-dimensional finite-difference time-domain (3D-FDTD) method with the FDTD software package from Lumerical Solutions, Inc. The x-axis polarized electromagnetic wave was set to propagate normal to the substrate (-z direction) for reflection, transmission, and near-field simulations. A perfect matching layer (PML) was applied to the boundary conditions in z-axis to eliminate any interference from the boundaries. In addition, PML and a periodic boundary were applied at x- and y-axes for simulating single and array nano-structures respectively.

4.3.4 SERS measurement

A Renishaw PL/Raman micro-spectroscope system was applied for SERS signal measurements. There were 633 nm He-Ne lasers with the power of 5 mW used as the excitation light source. A 20X objective lens (NA = 0.45) was used to focus/collect incident light and Raman signal

onto/from the surface of FlexBrite. The range of the collected wavenumbers was from 200 to 2000 cm^{-1}. The laser power was attenuated to 1.23 mW and 211 μW with neutral density filters. The methamphetamine solution, 1.0 mg/mL in methanol, ampule of 1 mL certified reference material and 1,2-bis(4-pyridyl)ethylene (BPE) were purchased from Sigma Aldrich.

4.3.5 Handheld Raman spectrometer

We used B&WTek NanoRam® handheld Raman spectrometer along with its software NanoRam® ID to measure the SERS spectrum of the methamphetamine solution. The vial adapter and a glass vial were used to contain the methamphetamine solution. The excitation laser wavelength is 785 nm; laser power is 5 mW. The spectral range is 176 cm^{-1} to 2900 cm^{-1}. The total data acquisition, averaging, background acquisition and post-processing took about two minutes.

4.3.6 Protocol for biotin-streptavidin binding

The following steps were used for functionalization of monolayer of biotin:

1. Rinse the FlexBrite with isopropanol followed by water then by isopropanol again.
2. Incubate the FlexBrite in thiolated-biotin solution (1 mM) for 24 hours at 37 ^{o}C.
3. Rinse the substrate with ethanol twice.

For biotin-streptavidin binding: Incubate the biotin-functionalized FlexBrite in streptavidin (1 μg/ml) for two hours. Thiolated biotin was purchased from Nanocs Inc. and stock solution was prepared with ethanol dilution. Streptavidin was purchased from Life Technology and stock solution is prepared with 1X PBS.

4.4 Conclusion

In this work, we demonstrated a novel dual-mode plasmonic and SERS substrate with large-area uniformity, low cost and mass producibility. The plasmonic colorimetry was characterized with the sensitivity of 611 nm/RIU, which enabled the naked-eye detection of biotin-streptavidin interaction. The SERS enhancement factor was characterized as 6.85×10^7 in a dry state and 4.81×10^8 in a wet state. The SERS property significantly enhanced the sensitivity of the handheld Raman spectrometer to enable the easy and fast detection of a trace amount of the narcotic drug methamphetamine in drinking water.

4.5 Figures

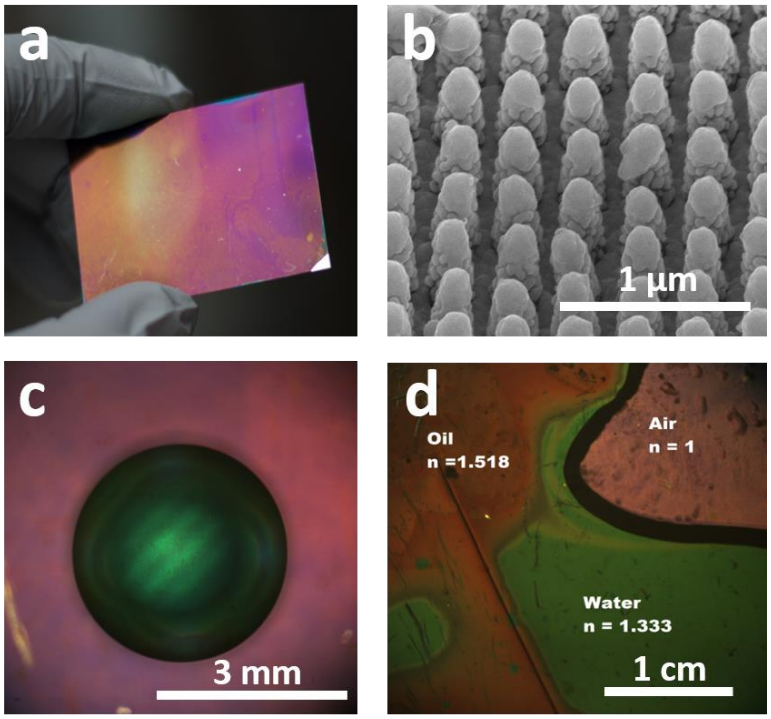

Figure 4.1 Overview of FlexBrite substrate. (a) Photograph of one piece of FlexBrite. (b) Scanning electron microscopy (SEM) image of surface of FlexBrite. (c) A water droplet on the surface of FlexBrite shows green color. (d) Water (n = 1) and cedar wood oil (n = 1.518) on the surface of FlexBrite show green and red color respectively.

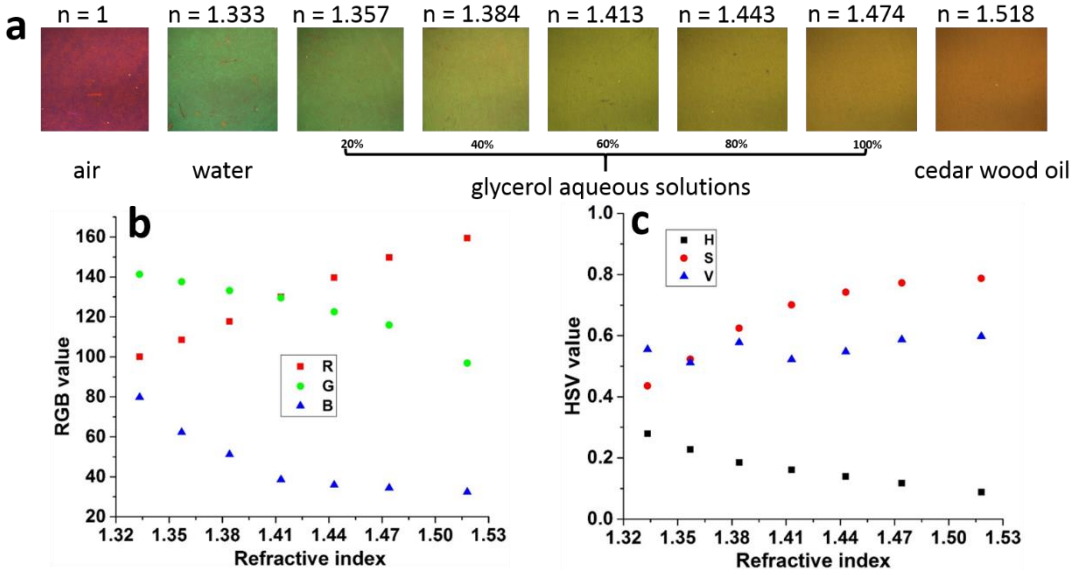

Figure 4.2 Plasmonic colorimetry with FlexBrite. (a) Images showing different colors with different refractive index (RI) of liquid on the surface. (b) Averaged RGB values with different RI of liquid. (c) Averaged HSV values with different RI of liquid.

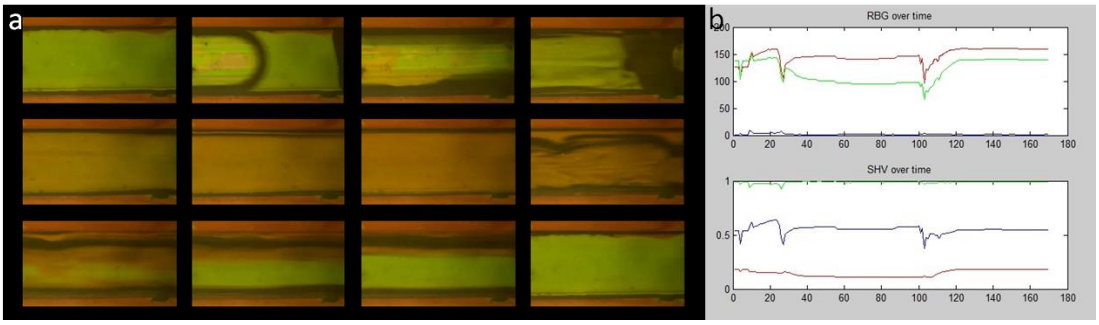

Figure 4.3 (a) A series of video snapshots to demonstrate the reusability of FlexBrite in microfluids. In a microfluidic channel (width = 500 µm) with FlexBrite in the bottom, water is first replaced with glycerol then glycerol is replaced with water again. (b) RGB (upper graph) and HSV (lower graph) values change of FlexBrite with time when alternatively replacing the liquid with water and glycerol.

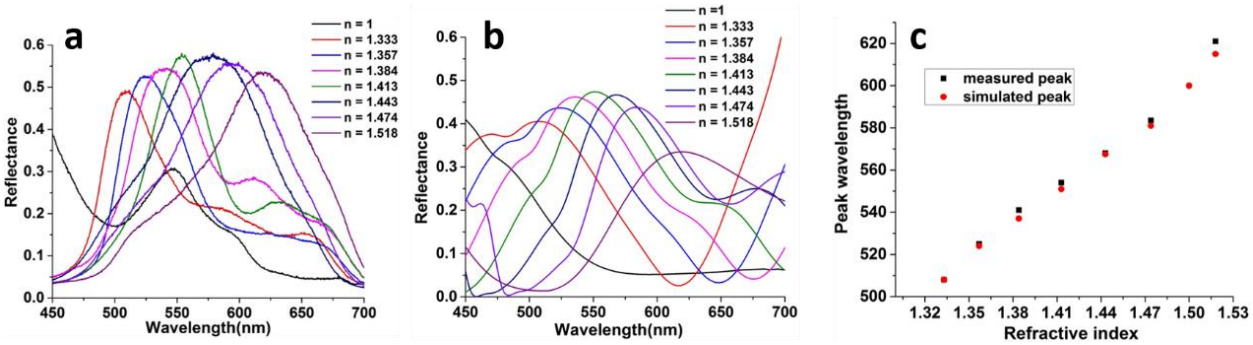

Figure 4.4 Spectroscopic characterization of FlexBrite. (a) Measured reflection spectra of FlexBrite with different RI of liquid. (b) Simulated reflection spectra of FlexBrite with different RI of liquid. (c) Measured (black) and simulated (red) reflection peaks with different n of liquid. Characterized sensitivity: 611 nm/RIU.

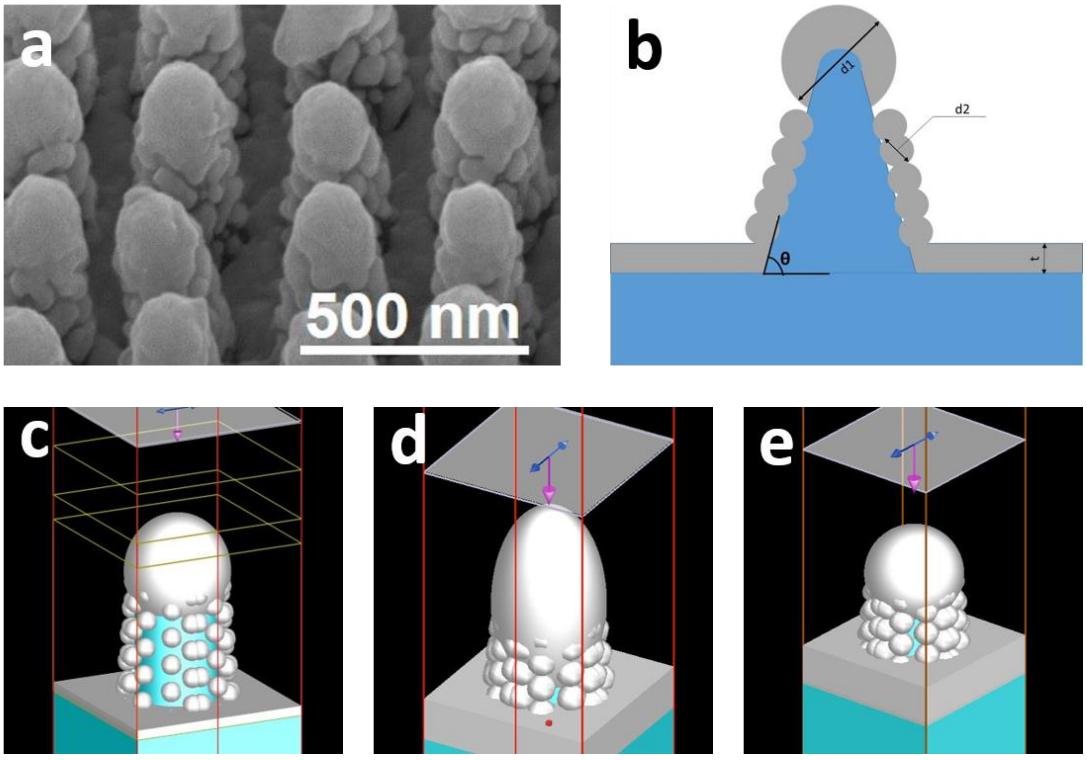

Figure 4.5 Optimization of FDTD simulation for reflection peaks of FlexBrite with different RI of liquid. The simulated structure parameters such as mushroom width, mushroom height, and size of the silver nanoparticles were calibrated using particle swarm optimization, so that the simulated reflection spectrum matched the peak and trough locations of the experimental data. (a) SEM image of nano-mushroom structure on the surface of FlexBrite. (b) Schematic of the FDTD model of nano-mushroom and the parameters used in optimization. (c-d) Snapshots of FDTD models with different parameters in optimization. (e) The optimal geometry with the simulated reflection peaks closest to the measured reflection peaks.

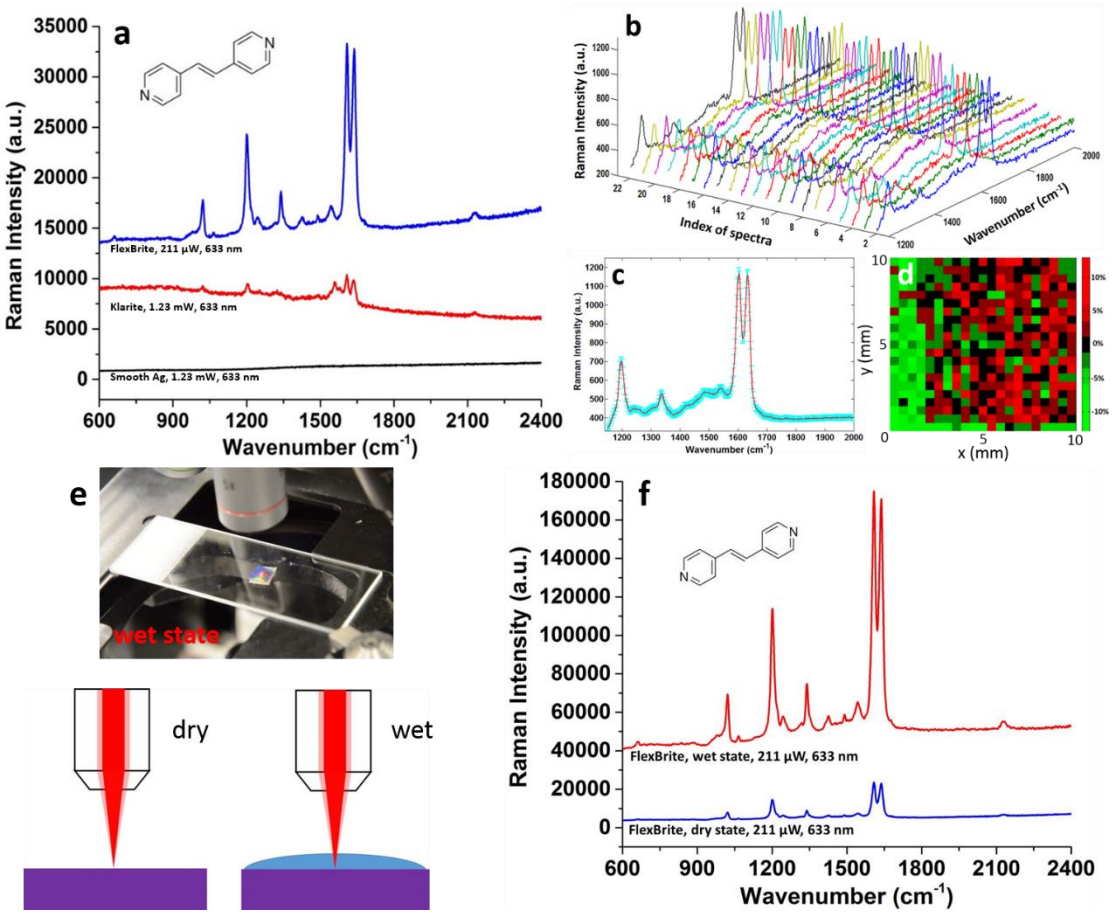

Figure 4.6 Surface-enhanced Raman spectroscopy (SERS) characterization of FlexBrite using 1,2-bis(4-pyridyl)ethylene (BPE) as the target molecule. (a) SERS comparison of FlexBrite, Klarite and smooth silver. (b) A series of SERS spectra of BPE at different spots on FlexBrite. (c) Averaged SERS (red curve) spectrum and standard deviation (cyan shadow) of BPE on FlexBrite. (d) Uniformity testing of SERS of BPE on FlexBrite by Raman mapping. (e) Illustration of dry state SERS and wet state SERS on FlexBrite. (f) Comparison of dry state SERS and wet state SERS of BPE on FlexBrite.

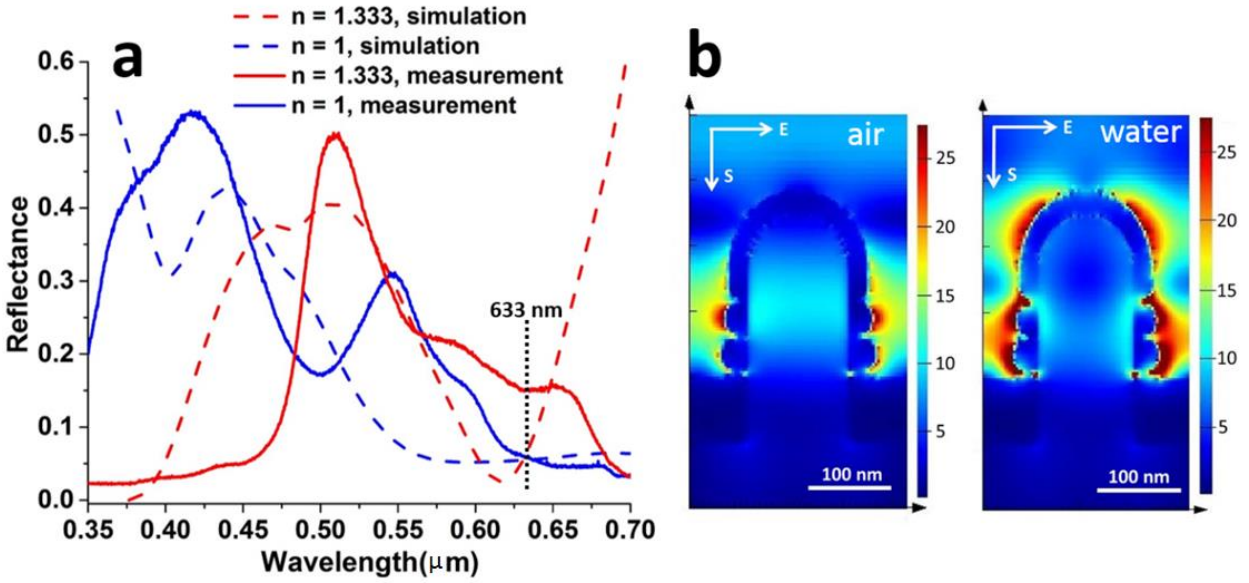

Figure 4.7 Explanation of stronger SERS of FlexBrite in wet state. (a) Measured (solid curves) and simulated (dashed curves) of FlexBrite in dry state (blue curves) and wet state (red curves). Both measured and simulated reflection spectra show a dip around 633 nm, the excitation laser wavelength. This indicates the resonance at 633 nm. (b) Electric field distribution of the simulated nano-mushroom in dry state (left, RI = 1) and wet state (right, RI = 1.33).

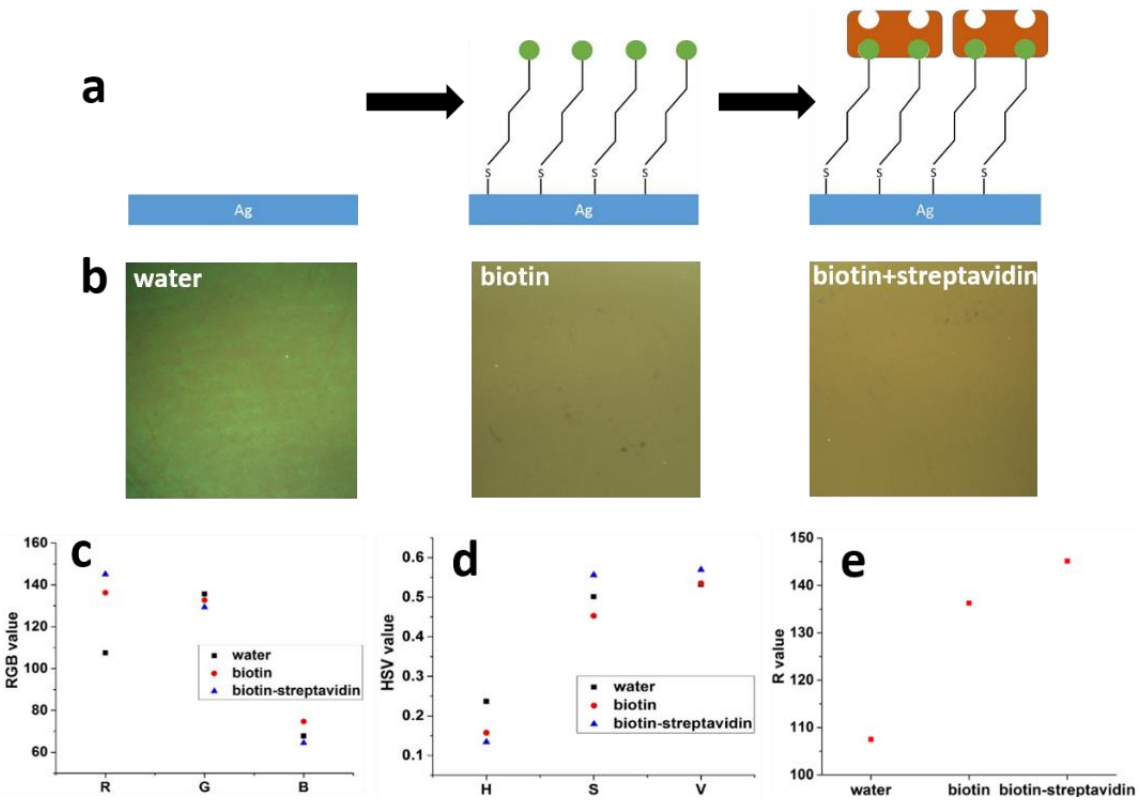

Figure 4.8 Detection of antibody-antigen reaction (biotin-streptavidin binding) with plasmonic colorimetry of FlexBrite. (a) The process of functionalization of thiolated biotin on the surface of FlexBrite and conjugation with streptavidin. (b) Colors of FlexBrite in wet state with water, after functionalization of thiolated biotin and after binding biotin with streptavidin. (c) Averaged RGB values of FlexBrite with water, biotin and biotin-streptavidin. (d) Averaged HSV values of FlexBrite with water, biotin and biotin-streptavidin. (e) Averaged R value of FlexBrite with water, biotin and biotin-streptavidin.

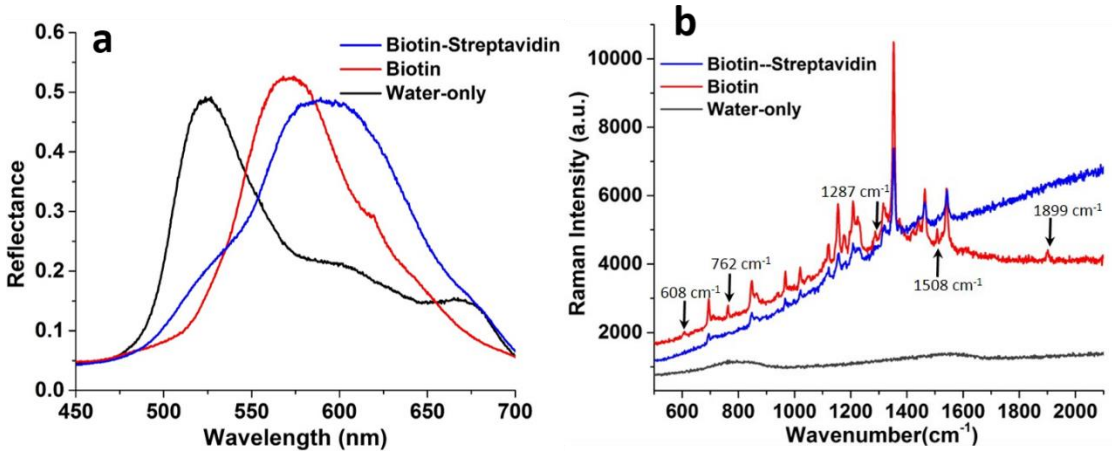

Figure 4.9 (a) Reflection spectra of FlexBrite with water, biotin and biotin-streptavidin conjugate on the surface of FlexBrite. (b) SERS spectra of FlexBrite with water, biotin and biotin-streptavidin conjugate on the surface of FlexBrite.

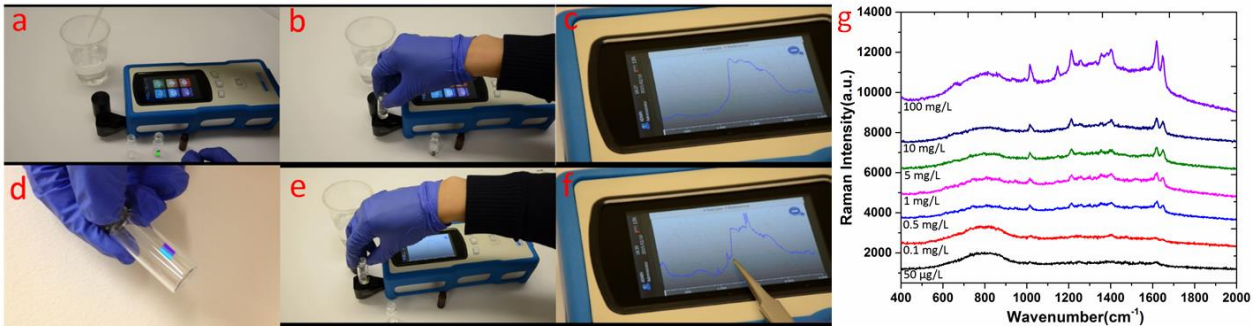

Figure 4.10 (a-f) Snapshots of a video to demonstrate the improved sensitivity of B&WTek NanoRam handheld Raman spectrometer with FlexBrite. (a) Diluting methamphetamine in water with the concentration of 1 mg/L (1 ppm). (b) Taking 1 ppm methamphetamine solution into the glass vial without FlexBrite for measurement with NanoRam spectrometer. (c) No Raman peaks were observed for 1 ppm methamphetamine solution without FlexBrite. (d) The glass vial with one piece of FlexBrite attached on the inner wall, facing outside. (e) Taking 1 ppm methamphetamine solution into the glass vial with FlexBrite for measurement with NanoRam spectrometer. (f) Raman peaks of methamphetamine were observed for 1 ppm methamphetamine solution with FlexBrite. (g) SERS of different dilutions of methamphetamine in aqueous solution. Limit of detection is 0.5 mg/L.

CHAPTER 5: 3D GOLD SERS SENSOR OPTIMIZATION

5.1 Introduction

Nowadays, the concerns of food safety, the demands of medical diagnostics, and the needs for environment monitoring, all require a low-cost and well-performed sensor for qualitative and quantitative measurements.[55,96–101] Compared with most other sensing technologies, optical sensors have the advantages of great sensitivity, wide dynamic range, electrical passiveness, freedom from electromagnetic interference, multiplexing capabilities, and a contact-free feature with which contamination can be avoided. However, the chemical fingerprint signal detected by regular Raman spectroscopy is very weak. Since 1973 when Martin Fleischmann et al.[102] observed Surface-Enhanced Raman Scattering (SERS) from roughened silver, researchers have developed different SERS substrates.

A synthesized or self-assembled noble metal nano-structure is commonly investigated but limited by its non-uniform enhancement factor and low consistency,[103,104] when researchers added patterned nano-structure by e-beam lithography on the substrate to achieve better uniformity of SERS enhancement or stronger surface coupling, the cost is too high for real application or mass-production;[105–107] some researchers fabricated a random nano-conic structure with low-cost reactive ion etching (RIE) and coated it with metal to achieve ~10^8 enhancement factor (EF)[16,108], but this process is hard to control and thus the quality of this kind of SERS substrates varies.Similar results were achieved with nano-sphere lithography where nano-spheres over large area could form additional unwanted gaps inevitably.[109]

To achieve a balance among cost, quality, and performance, researchers started with a nano-patterned stamp and leveraged a nano-replica technique to fabricate multiple samples at low

cost,[110–116] because structures from this process have better consistency during fabrication, which ensures quality, and they have strong coupling due to their small gaps between adjacent nano-domes or nano-particles. These nano-structures have unique plasmonic properties leading to surface plasmon resonance (SPR) and localized surface plasmon resonance (LSPR).[117–119] It has been reported that a silver-coated nano-structure forming small gaps has strong SERS EF.[120] However, it is well known that silver is not bio-compatible, and even silver nano-particles have been applied for anti-bacterial purposes.[121] In addition, silver degrades by oxidation in the air over time so that the lifetime for silver-based SERS devices at high EF is limited. Instead, gold-based SERS devices with good bio-compatibility and high stability are favorable in the industry, and that is why Klarite SERS substrate is called the gold standard for SERS although it has EF of only 10^6.[122]

Previously, our group has demonstrated a wafer-scale, dual-mode plasmonic colorimetry and SERS substrate based on plastics, named FlexBrite.[123] In this dissertation, starting from the replica of the same nano-stamp for FlexBrite, we tuned the gaps between nano-pillars by sputtering SiO_2 of different thicknesses. After coating gold, the distance between gold nanoparticles decreased. As a result, we increased the EF by 3.4 times. Measurement and simulation have been performed to explain the improvement.

5.2 Methods

5.2.1 Fabrication process

The nano-mushroom structure of FlexBrite was fabricated by a nano-replication process with a 4-inch SiO_2 master mold. Like what we did previously in Fig. 6S by Zhida Xu[123] or Fig. 1 by Te-wei Chang,[111] where the cross-sectional schematic of the fabrication process was demonstrated. After

we got the nano-pillar array by molding the nano-cup array with Norland Optical Adhesive 61 (NOA 61), we sputtered SiO_2 of different thicknesses using K. J. Lesker PVD 75 system as Fig. 5.1 (a, b) show. With Gaertner L116C ellipsometry, we measured the thickness of sputtered SiO_2 on planar area. Since sputtering process is non-directional, there will be some coverage on the sidewalls of the nano-pillars but they are still thinner than on the planar area. And the thickness of SiO_2 in Fig. 5.1 (b) is thicker than Fig. 5.1 (a) where Fig. 5.1 (a, b) show the schematic for plastic nano-pillar coated with a thin and thick layer of SiO_2, respectively. After coating different thicknesses of SiO_2, we used CHA SEC-600 to coat 9 nm of titanium and 90 nm of gold by e-beam evaporation. The titanium layer was coated for better adhesion. The nano-mushroom structure was formed after metal deposition where the top and bottom of the nano-pillar have thicker gold and the sidewalls have close-packed gold nano-particles as Fig. 5.1 (c, d) illustrate. Figure 5.1 (c, d) show the sample after metal coating onto the substrate of Fig. 5.1 (a, b) respectively. And the results observed with scanning electron microscopy (SEM) of nano-mushroom with SiO_2 thicknesses ranging from 20 nm to 120 nm are shown in Fig. 5.1 (e-j). From these images, we observed that with thicker SiO_2 deposition, the gaps between nano-mushrooms are smaller. Also, the nano-particles on the sidewalls of nano-pillars can be observed clearly, and their distributions are consistent in each picture. After the metal coating, we cut a rectangular piece from the 4-inch plastic wafer and take a picture as Fig. 5.1 (k) shows. The wafer is flexible, lithography-free, and can be manufactured at high throughput and low cost. FlexBrite also shows many rainbow colors due to the grating effect.

5.2.2 FDTD simulation

We used the commercially available 3D-FDTD software (Lumerical Solutions, Inc) to simulate the structure. The x-axis polarized electromagnetic wave was set to propagate toward to the

substrate (-z direction) for near-field and reflection simulations. A perfect matching layer (PML) was applied to the boundary conditions in z-axis to eliminate any interferences from the boundaries. In addition, periodic boundary condition was applied at x- and y-axes to simulate a 2D-array of nano-structure.

5.2.3 SERS measurement

A SERS signal was measured with Renishaw PL/Raman micro-spectroscope system. A 633 nm He-Ne laser with the power of 5 mW was used as excitation. A 20X objective lens (NA = 0.45) was used to focus and collect incident light and the Raman signal from the surface of the substrates. The wavenumber range is from 1170 to 1950 cm^{-1}. Neutral density filters were applied to attenuate the laser power to 1.23 mW and 211 µW. A solution 1,2-bis(4-pyridyl)ethylene (BPE) was purchased from Sigma Aldrich. Before the measurement, a nano-mushroom substrate was cut into small pieces and soaked in BPE solution for six hours. Then a monolayer of BPE was formed on the nano-mushroom sensor substrate. Measurement was done in both dry and wet conditions. For the dry condition, we took the sample from the BPE solution and put it on a piece of glass slide; while at the wet condition, after finishing the steps for the dry condition, we dropped 20 µL of DI water on top of the sample, then covered it with a piece of cover slip.

5.2.4 Calculation of SERS enhancement factor (EF)

The average of SERS enhancement factor (EF) from the FlexBrite sensor can be calculated based on the following equation:

$$EF = \frac{I_{SERS}}{I_{Raman}} \times \frac{N_{Raman}}{N_{SERS}} \times \frac{P_{Raman}}{P_{SERS}} \times \frac{T_{Raman}}{T_{SERS}} \quad (5.1)$$

where I_{SERS} and I_{Raman} are integrated scattered intensities of a Raman signal from a FlexBrite sensor and BPE bulk solution. N_{SERS} and N_{Raman} are the numbers of molecules being probed in the FlexBrite sensor and in the BPE bulk solution. P_{SERS} and P_{Raman} are the power intensities of the excitation laser applied onto the FlexBrite sensor and BPE bulk solution. T_{SERS} and T_{Raman} are the acquisition times when measuring the Raman signal on the FlexBrite sensor and in the BPE bulk solution. I_{SERS} and I_{Raman} were measured with the integrated peak intensity at wavenumber 1607 cm^{-1}.

5.2.5 Reflectance spectrum measurement

An Olympus BX51 upright microscope was used to measure the reflectance spectrum with USB2000+. For the measurement, after we recorded the spectrum of the light source reflected by a silver mirror going into the object lens and the spectrum for the dark environment, we placed the sample on the stage of the microscope and measured the reflection spectrum of each sample.

5.3 Results

5.3.1 SERS characterization

To measure the SERS properties of modified FlexBrite, we used 1,2-bis(4-pyridyl)ethylene (BPE) to form a uniform monolayer on the gold surface after incubation. For surface functionalization with BPE, FlexBrite was immersed in 100 µM BPE solution diluted with ethanol for six hours and then rinsed in pure ethanol, followed by blow drying with nitrogen to ensure a uniform single-molecular layer adsorbed on the surfaces.[85] The Renishaw Raman spectrometer with a He-Ne laser of 633 nm excitation wavelength and 20X objective lens was used for the Raman spectroscopy measurement.

Figure 5.2 (a) shows the SERS measurement of FlexBrite with different SiO_2 thickness at the dry state. With the same laser power and integration time for excitation, we found that the SERS signal increases by 2.6 times with 120 nm thickness of SiO_2 compared with thin SiO_2 deposition. At the wet state, we have the measurement result in Fig. 5.2 (b) showing that the SERS signal increases by 3.4 times with 120 nm thickness of SiO_2 compared with the sample with thin SiO_2 deposition. Figure 5.2 (c) shows the side view of a 3D illustration with FlexBrite of different SiO_2 thicknesses. Since the periods of the nano-pillars on different samples are the same, thicker deposited SiO_2 means the smaller gaps between the nanoparticles in adjacent nano-mushrooms, resulting in stronger LSPR coupling between adjacent nano-mushrooms and better SERS signal which will be explained in the Section 5.3.2. The Raman enhancement factor (EF) was calculated by comparison of the SERS signal intensity.[123] By considering the primary peak height at 1618 and 1648 cm^{-1}, we calculated the SERS EF for different tuning parameters and plotted them in Fig. 5.2 (d).

From the measurement results, we can see that the EF of FlexBrite at the wet state is lower than at the dry state with a thin SiO_2 layer because the glass slide reflected partial power from the incoming laser beam. But as the thickness of SiO_2 increases, the EF at the wet condition increased faster than the dry one. Thus, the SiO_2 sputtering can improve the SERS EF at the wet condition more significantly.

To verify the enhancement effect from FlexBrite, we also measured the SERS of gold nanoparticles (AuNPs) of 50 nm with the same concentration of BPE, laser excitation power and exposure time. The solution of gold nanoparticles (50 nm, EM.GC50 purchased from BBI Solutions) is dropped on a piece of silicon wafer. After the solution evaporates, the sample is ready to use. From Fig. 5.3 (a, b), one can clearly see that the AuNPs are either multilayer packed or sparsely distributed in forms of aggregations. The SERS result is shown in Fig. 5.3 (c). It turns out the SERS signal of

FlexBrite is 22 times stronger than AuNPs at the dry state and 14 times stronger than at the wet state on average. This shows that FlexBrite contributes as a higher-quality substrate in terms of both uniformity and signal strength.

5.3.2 FDTD modeling and simulation

To understand the mechanism of FlexBrite's SERS EF improvement when coating SiO_2 with different thicknesses, we used a FDTD method to simulate the electric field distribution and reflectance spectra with nano-structures corresponding to FlexBrite. After observing the nano-structure of FlexBrite from the SEM image in Fig. 5.1 (e-j) we understand that the polymer nano-pillars are covered with a large hemi-ellipsoidal gold on top and many close-packed small gold nano-particles on the sidewall. To explain the SERS enhancement from these structures, we believe that the LSPR effect comes from the nano-particles on the sidewall of each single nano-pillar while the periodic structure of the nano-pillars contributed to the SPR enhancement.[75,120,124–128] After we sputtered thicker SiO_2 before coating gold, the spacing between adjacent pillars became smaller. As a result, we enhanced the coupling between the gold nano-particles and between adjacent pillars while keeping all the other structures for LSPR and SPR the same. Meanwhile, since we coated with the same thickness of gold for all the cases, the formation of gold nano-particles on the sidewall of each scenario is almost the same.

In addition, because the structure of the nano-particles on the sidewall is randomized, the simulation for FlexBrite is not trivial. After tuning the shape, size, and distribution of the sidewall particles with a similar method in our previous research,[123] we have five models whose thickness of SiO_2 were 0 nm, 10 nm, 20 nm, 30 nm, and 40 nm, respectively. In Fig. 5.4 (a-c) the 0 nm, 20 nm, and 40 nm models of nano-mushroom were plotted. The reason we modeled with thinner SiO_2 than the ones in the experiment is that the thicknesses in the latter case are measured along

the vertical direction and the actual coverages of SiO_2 on the sidewalls of nano-pillars are much thinner. In the simulation model, the thicknesses of SiO_2 are perpendicular to the surface of the sidewalls of the nano-pillars. By comparing Fig. 5.4 (c) with Fig. 5.1, we know that the nano-mushroom with 40 nm-thick SiO_2 in simulation model have similar structure with 120 nm sample during experiment. Also if the thickness of SiO_2 is higher, the adjacent nano-mushrooms will touch each other. After running the FDTD simulation for each case at the dry condition where the refractive index of the surrounding region is 1 and the wet condition where the refractive index of surrounding area is 1.333, we have figures of Fig. 5.4 (d-h) with 633 nm incident light showing the electric field of the cross-section view of the nano-mushroom along the x-axis (E-field polarization) direction. For fair comparison, we normalized the max intensity of the magnitude of field to be 6 (power of the electric field to be 36) for all simulation results. From the simulation results, we can observe that the field gets stronger when the SiO_2 is thicker, induced by the smaller spacing between adjacent pillars, while the electric field at the wet condition is stronger than the one at the dry condition. This agrees with our observation for SERS measurement except that the electric field is for FlexBrite with a thin SiO_2 substrate at the wet condition is stronger than the dry condition, however the SERS signal at the wet condition is weaker. We believe this is because the cover slip we used at the wet condition attenuates both the incoming laser beam and the excited Raman signal.

5.3.3 Reflectance measurement and simulation

With a previously described method for reflectivity measurement, we achieved dark field intensity of the spectrometer with the light source off, the control spectrum with a silver mirror reflecting the incoming light from the light source, and the reflected signal with our FlexBrite sensors. Using these parameters, we can calculate the reflectivity. With the reflectivity is

normalized by its largest value as 1, the reflectivity of FlexBrite with different SiO_2 thicknesses at dry and wet conditions are plotted in Fig. 5.5 (a, b).

From the measurement, we observed a trend of red-shift as SiO_2 thickness increases. When we plotted the peak wavelength of each curve in Fig. 5.5 (c) it showed that at the dry condition the peak wavelength increased linearly, while the one at the wet condition also increased more or less although with some fluctuation. Furthermore, we ran a set of simulation based on the model introduced in Section 5.3.2. We added a monitor to observe the energy reflected from the nano-mushroom structures. After normalization, we plotted the reflectance of the dry and wet conditions in Fig. 5.5 (d, e). Here the reflectivity curves were generated with a little randomization of the gold nano-particles along the nano-pillars to avoid the grating effect which gave high-frequency oscillating reflectance curves. For the dry condition, the normalization used the peaks around 0.55 μm as 1; for the wet condition, the normalization used the maximum reflectance from 0.45 μm to 0.7 μm as 1. When we plotted the peak wavelength of each case in Fig. 5.5 (f), we can see a steady increase of the peak wavelength for dry and wet conditions. The reason we used the peak around 0.55 μm for normalization for the dry condition is that during our experiment, the light source only has a visible range and the intensity below 450 nm or above 670 nm was very weak and not reliable. Thus, the reflectance at those regions is not reliable. As a result, the high reflectivity above 0.6 μm was not shown consistently in the measurement.

Meanwhile, as we discussed before, the simulation for the nano-mushroom structure is not trivial, so we can hardly achieve a perfect simulation matching the experiment exactly. However, we can still see the key features that match the experiment and explain the phenomena. According to literature,[129] the smaller spacing between metal nano-particles will result in a red-shift of the reflectance spectrum due to the LSPR effect. Although there is some discrepancy between the experimental and FDTD simulation results consequently, the SERS intensity generally follows the

plasmon ruler principle and shows an exponential dependence on the gap between the nano-mushrooms. This matches with our experiment result. The limited change is because only the spacing between adjacent nano-particles changed while the ones on the same nano-pillar stay at the same relative location with each other. To correlate the relationship between the reflectance spectrum and the SERS improvement when SiO_2 thickness increases, we can observe that in Fig. 5.5 (d), a reflection dip is formed at around 633 nm which means that stronger SPR coupling is created with thicker SiO_2 coating.[130,131] We can also observe a similar dip at dry state measurements with thicker (100 nm) SiO_2 in Fig. 5.5 (a).

To further analyze the LSPR and SPR effect from the nano-mushroom structure, we have performed FDTD simulations to calculate the reflection spectra with different incident angles, as shown in Fig. 5.6 In this dissertation, the reflection dips signify the occurrence of plasmonic resonance. The dip values of reflection spectra are summarized in Table 5.1. At normal incidence, we can observe two reflection dips at 550 nm and 673 nm, respectively. When the incident angle increased from 0^o to 67.5^o, the reflection dip at 550 nm remains almost unchanged, which is ascribed to the LSPR of the gold-coated nano-pillars.

However, the reflection dip at 673 nm is slightly shifted to 685.5 nm with the increasing incident angle. As a result, we conclude this dip is at a longer wavelength as the hybrid plasmon resonance, induced by the coupling between the SPR on the air-gold interface excited by the periodic pillars and the strong scattering effect of the nanoparticles, and the LSPR. In addition, at a large incident angle (67.5^o), it is also possible to excite the SPR on the sidewall of the nano-mushroom, which can propagate between different nanoparticles. Since the structure of the nano-mushroom is much more complicated compared with the nano-dick array in R. Nicolas et al.,[132] it is hard to predict the wavelength.

5.4 Discussion

5.4.1 Significance of this research

In order to produce a real-world usable product with nanotechnology, we need to consider both performance and cost. When working with nano-scale structures in the lab, cost can be greatly reduced with nano-replica method[112] compared with electron beam lithography or other nano-fabrication techniques. Moreover, the process for preparation of the samples can be done outside of a cleanroom. In this chapter, we used nano-replica methods as a technique to mass-produce our working sensors at low cost and high performance.

In previous literatures,[109,112] researchers changed the gaps between nano-domes or nano-spheres to improve the coupling between adjacent spheres at 2D scale. In this dissertation, what we decreased was the distance between each pair of the nano-pillars each of which has an array of nano-particles. Thus, we improved the coupling between nano-spheres at 3D scale in this chapter.

Furthermore, during research at the nanoscale, in order to lower the cost, researchers cannot rely on e-beam lithography for all their samples and most labs do not have a deep UV lithography system for sub-500 nm structure. Previously, some groups have applied nano-replica methods to reduce the cost of research and used simulation tools to predict the performance when changing the geometrical structure.[112] However, due to the complexity of the geometry, simulation cannot always predict an accurate result. Making too many templates with e-beam lithography consumes too much time and too many resources. This dissertation used a low-cost method that is to sputter SiO_2 on top of the nano-structure and investigate the performance of our devices. Similar methods can be applied to other scenarios.

5.4.2 Potential application

As we know that silver-coated nano-patterns provide a strong SERS signal. However, silver is not bio-compatible. Further, the gold-based SERS substrate is limited by its weak SERS effect. In this dissertation, we improved the performance of the gold-based SERS substrate by 3 times after a simple process by tuning the nano-pillar structure with SiO_2 sputtering and increasing the LSPR coupling. Thus, researchers can use this substrate to observe the Raman signal of biology samples and preserving their bio-activity. In addition, with this method, we achieved a SERS substrate with a performance 15 times better than the gold standard Klarite at a cost of 5%.

5.5 Conclusion

In summary, we presented the fabrication, design, and test of an improved the gold-based SERS substrate that can be manufactured at wafer-scale. With the fine-tuning of oxide thickness, we achieved a 3.391 times improvement and an enhancement factor of 1.55×10^7 which is 15 times higher than the current gold standard of the SERS substrate, Klarite. Simulation was performed to explain the improvement with LSPR and SPR theory.

5.6 Figures and table

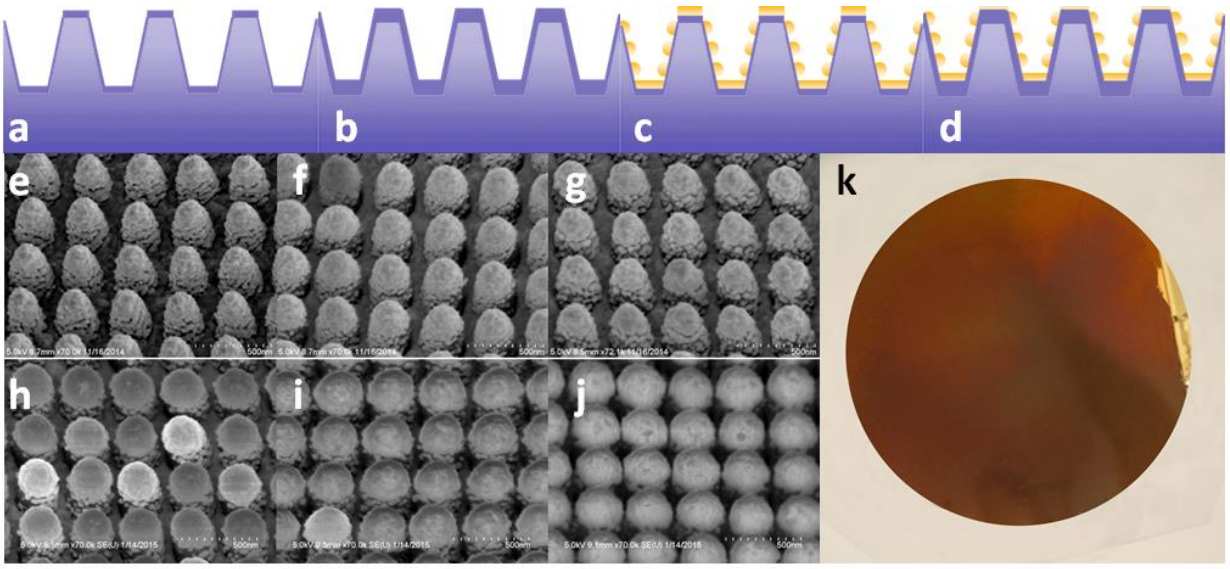

Figure 5.1 (a) Schematic for plastic nano-pillar coated with a thin layer of SiO_2. (b) Schematic for plastic nano-pillar coated with a thick layer of SiO_2. (c) Schematic for 9 nm Ti and 90 nm Au coated on (a). (d) Schematic for 9 nm Ti and 90 nm Au coated on (b). (e-j) SEM image of nano-mushroom after metal coating with SiO_2 thickness of 20 nm, 40 nm, 60 nm, 80 nm, 100 nm, and 120 nm. The scale bar is 500 nm and the image was taken at 20^{o} slanted view. (k) Photograph of one piece of FlexBrite sample cut from a 4-inch plastic wafer.

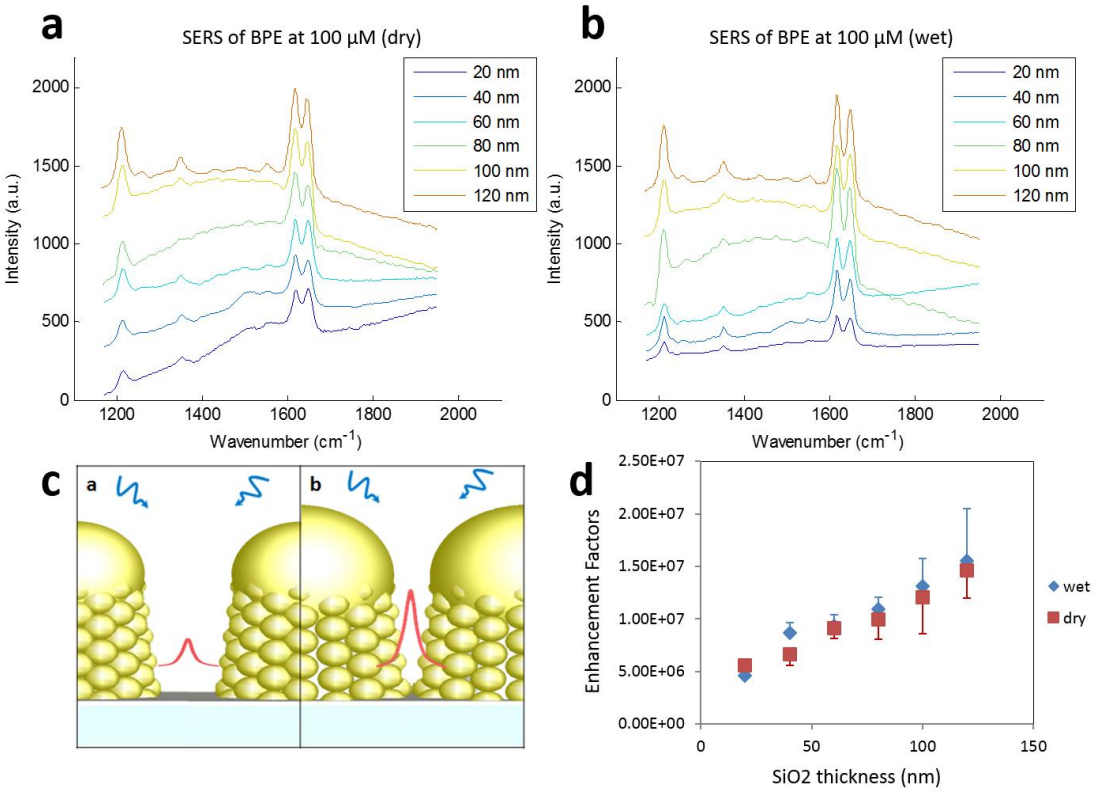

Figure 5.2 (a) SERS measurement of FlexBrite with different SiO_2 thickness at dry state. The legend is the thickness of SiO_2 of each sample. (b) SERS measurement of FlexBrite with different SiO_2 thickness at wet state. The legend is the thickness of SiO_2 of each sample. (c) Side view of 3D nano-mushroom with 0 nm SiO_2 (left) and 40 nm SiO_2 (right). It signifies that when the excitation laser (blue) shines on the FlexBrite substrate, the left sample produces a weak Raman signal (red) while the right sample produces a strong Raman signal (red). (d) The enhancement factor of each sample in dry (red) and wet (blue) states with different thicknesses of the SiO_2 layer with the error bars plotted.

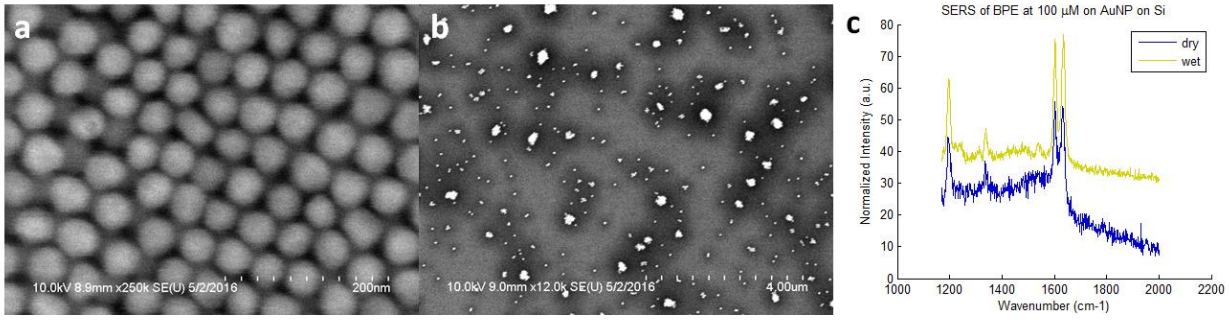

Figure 5.3 (a, b) SEM of 50 nm gold nanoparticle on silicon at different locations where (a) has multi-layer, (b) has sparse distribution with aggregation. (c) Average SERS signal of BPE (100 µM) on AuNP sample at dry and wet state.

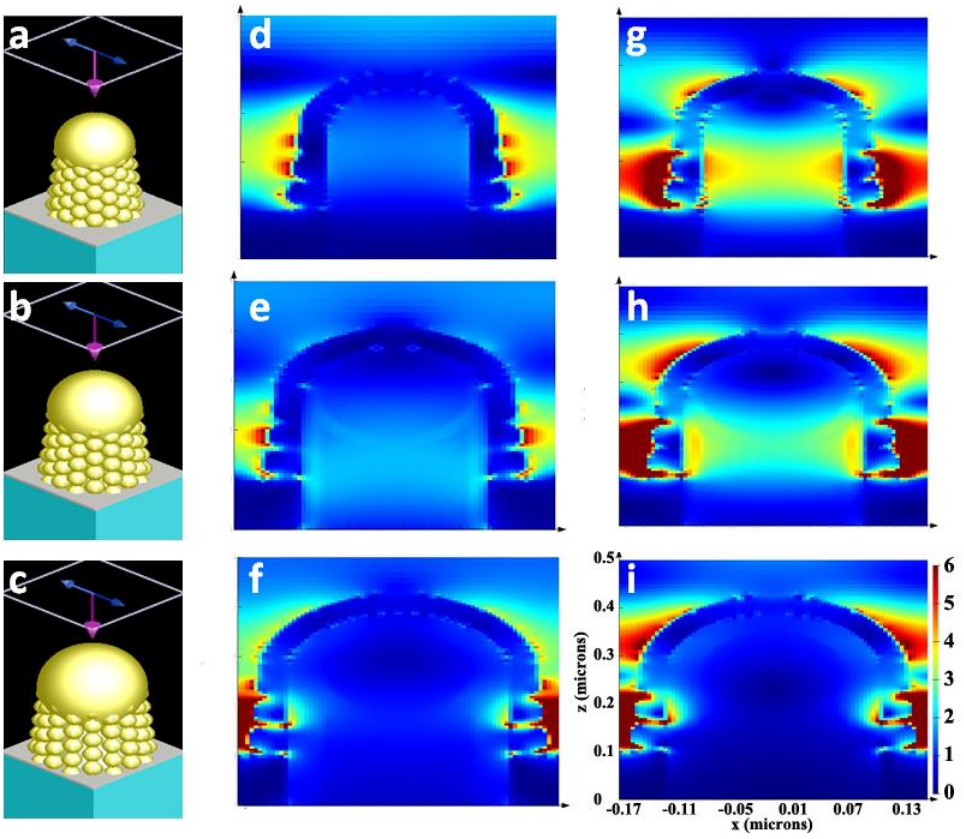

Figure 5.4. (a-c) The FDTD model of nano-mushroom with the SiO_2 thickness of 0 nm (a), 20 nm (b), 40 nm (c) respectively. (d-f) Electric field monitor result with the incident wavelength is 633 nm with the SiO_2 thickness of 0 nm (d), 20 nm (e), 40 nm (f) respectively at dry state. (g-i) Electric field monitor result with the incident wavelength is 633 nm with the SiO_2 thickness of 0 nm (g), 20 nm (h), 40 nm (i) respectively at wet state.

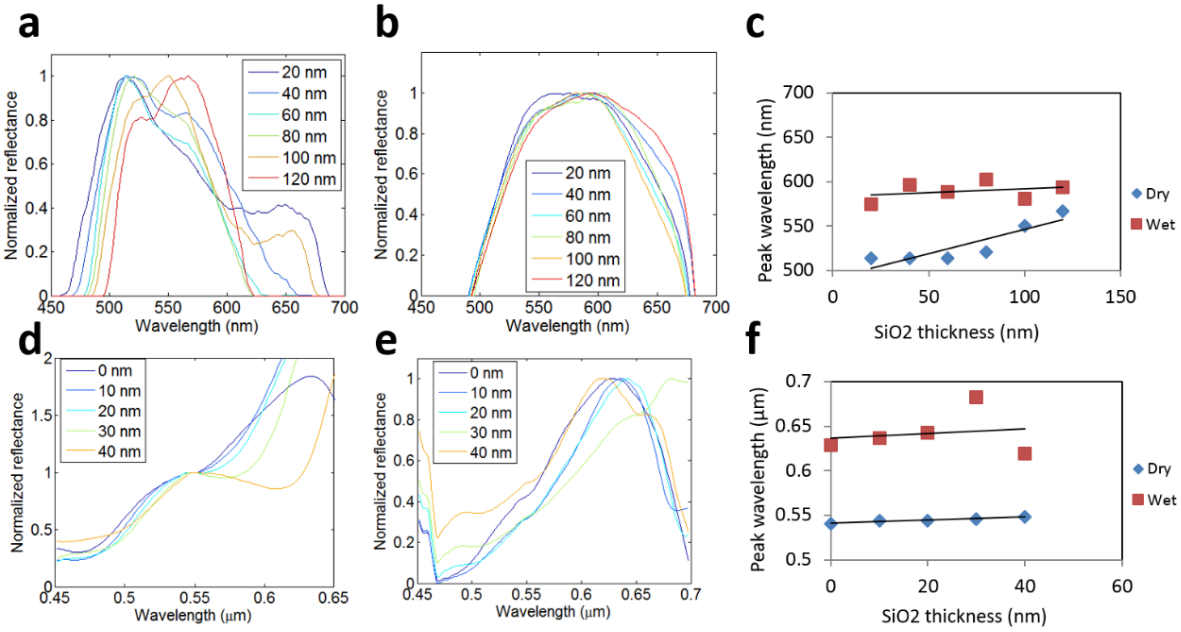

Figure 5.5 (a, b) Measurement of reflectance (after normalization) over wavelength of samples with different SiO_2 thickness at dry (a) and wet (b) state. (c) Peak wavelength over SiO_2 thickness from sample reflectance measurement. (d, e) Simulation of reflectance (after normalization) over wavelength of samples with different SiO_2 thickness at dry (d) and wet (e) state. (f) Peak wavelength over SiO_2 thickness from simulation.

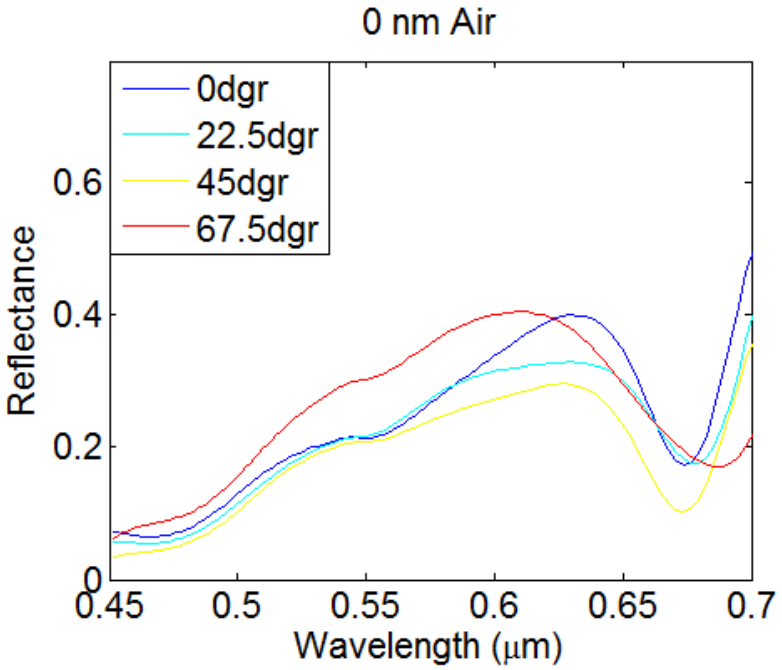

Figure 5.6 Simulation of reflectance with different incident angle.

Table 5.1 Dip wavelength of reflection spectra

Angle (°)	Dip1 wavelength	Dip2 wavelength
0	548.2 nm	670.5 nm
22.5	546.2 nm	673.4 nm
45	546.2 nm	670.5 nm
67.5	546.2 nm	685.5 nm

CHAPTER 6: CONCLUSION AND FUTURE WORK

6.1 Conclusion

This dissertation includes two types of sensor design: one for impedance-based bacteria sensing, another for SERS sensing. Both sensors are highly sensitive, low cost, flexible, mass-producible. As the bottleneck preventing broader application of portable sensing, this work has provided a proof-of-concept study to combine theoretical studies and advanced fabrication practices to achieve well-performed sensor chips.

Specifically, starting from silicon-based through-hole impedance sensor with a pre-concentrating function, we demonstrated the ability to reach the detection limit of prior art[5] even before pre-concentrating. In the following dissertation, we replaced the difficult-to-fabricated silicon sensor by a filter-based sensor, combining it with a 3D printed scaffold and low-melting 3D printed filament confining the microfluidic channel, we lowered the sensor cost significantly. In addition, with further study of the Hook effect and improvement of the equivalent circuit model for paper-based impedance sensing, we further lowered the detection limit by to 5% of the previous work. Further, we developed a Bluetooth-based impedance sensing component that can be used with a smartphone to work with this sensor easily.

Meanwhile, a powerful characterization technique, Raman, has limited application due to the weakness of the signal. SERS, however, can amplify the Raman signal by millions of times. Gold standard SERS substrate, Klarite, is limited by its low sensitivity and high price. Because of this, we have developed a wafer-scale, flexible, polymer-based nano-pillar SERS sensor with an enhancement factor as high as 4.81×10^8 for the silver-based sensor. This achievement is not only benefited from our detailed study of the condition of optimal affinity between sensing targets and SERS substrate, but also due to the extended hotspots from the dense silver nanoparticles

along the nano-pillar. Furthermore, in the following work, we also fine-tuned the nano-pillar structure by sputtering an additional layer of SiO_2 at different thicknesses, so as to increase the EF by 3.4 times for the gold-coated sensor. Simulation and reflectivity measurement were performed for theoretically reasoning of the additional improvement of SERS. With this ultrasensitive, low-cost, and highly uniformed SERS substrate, we demonstrated the application with a handheld Raman spectrometer from B&WTek to for drugs detection in wine.

6.2 Future work

For the paper-based impedance sensor, firstly, the consistency across different sensor chips can be improved with the screen printing techniques. When we applied e-beam evaporation, the uniformity was not ideal because the shadow mask was deformed more or less during the evaporation process due to thermal expansion. Secondly, different applications and testing methods can be studied: for example, another member in our research group has used differential pulse voltammetry for blood cell sensing with paper-based microfluidics. That configuration can be simplified when incorporating the design in this work. In the end, a miniaturized portable smartphone-based impedance sensing module should be successfully accomplished. Due to the time limit and the shift of focus, we were not able to finish the testing based on our design.

For the SERS project, further improvement can be accomplished by research into the optimal condition for other to-be-detected targets. During this dissertation, the detectability of targets with different molecule sizes, hydrophobicity varies drastically. On the side of portable sensing, because the work in this dissertation has dual functions for SERS sensing and colorimetric sensing, a cost-effective portable device that can measurement both signals simultaneously can be beneficial.

REFERENCES

1. IDTechEx, http://www.idtechex.com/research/articles/the-next-generation-of-flexible-sensors-in-printed-electronics-00006245.asp, (accessed Jan 2017).
2. C. Pang, C. Lee and K. Y. Suh, *J. Appl. Polym. Sci.*, 2013, **130**, 1429–1441.
3. A. M. López-Marzo and A. Merkoçi, *Lab. Chip*, 2016, **16**, 3150–3176.
4. J. S. Daniels and N. Pourmand, *Electroanalysis*, 2007, **19**, 1239–1257.
5. L. Yang, Y. Li and G. F. Erf, *Anal. Chem.*, 2004, **76**, 1107–1113.
6. N. N. Watkins, U. Hassan, G. Damhorst, H. Ni, A. Vaid, W. Rodriguez and R. Bashir, *Sci. Transl. Med.*, 2013, **5**, 214ra170.
7. K. Kant, J. Yu, C. Priest, J. G. Shapter and D. Losic, *Analyst*, 2014, **139**, 1134–40.
8. D. Zhang and Q. Liu, *Biosens. Bioelectron.*, 2015, **75**, 273–284.
9. A. Nemiroski, D. C. Christodouleas, J. W. Hennek, A. a Kumar, E. J. Maxwell, M. T. Fernández-Abedul and G. M. Whitesides, *Proc. Natl. Acad. Sci. U. S. A.*, 2014, **111**, 11984–9.
10. P. B. Lillehoj, M.-C. Huang, N. Truong and C.-M. Ho, *Lab Chip*, 2013, **13**, 2950.
11. J. L. Delaney, E. H. Doeven, A. J. Harsant and C. F. Hogan, *Anal. Chim. Acta*, 2013, **790**, 56–60.
12. Z. V. Feng, I. L. Gunsolus, T. A. Qiu, K. R. Hurley, L. H. Nyberg, H. Frew, K. P. Johnson, A. M. Vartanian, L. M. Jacob, S. E. Lohse, M. D. Torelli, R. J. Hamers, J. Murphy and C. L. Haynes, *Chem. Sci.*, 2015, **6**, 5186–5196.
13. K. Kneipp, K. Kneipp, H. Kneipp, H. Kneipp, I. Itzkan, I. Itzkan, R. R. Dasari, R. R. Dasari, M. S. Feld and M. S. Feld, *Chem. Rev.*, 1999, **99**, 2957–76.
14. A. Campion and P. Kambhampati, *Chem. Soc. Rev.*, 1998, **27**, 241–250.
15. M. Kahraman, P. Daggumati, O. Kurtulus, E. Seker and S. Wachsmann-Hogiu, *Sci. Rep.*, 2013, **3**, 3396.
16. Z. Xu, J. Jiang, M. R. Gartia and G. L. Liu, *J. Phys. Chem. C*, 2012, **116**, 24161–24170.
17. M. R. Gartia, B. Braunschweig, T.-W. Chang, P. Moinzadeh, B. S. Minsker, G. Agha, A. Wieckowski, L. L. Keefer and G. L. Liu, *J. Environ. Monit.*, 2012, **14**, 3068–75.
18. L. Wang, Q. Liu, Z. Hu, Y. Zhang, C. Wu, M. Yang and P. Wang, *Talanta*, 2009, **78**, 647–652.
19. Q. Liu, H. Cai, Y. Xu, L. Xiao, M. Yang and P. Wang, *Biosens. Bioelectron.*, 2007, **22**, 3224–3229.
20. N. J. Ashbolt, *Toxicology*, 2004, **198**, 229–238.
21. X. Xue, J. Pan, H. Xie, J. Wang and S. Zhang, *Talanta*, 2009, **77**, 1808–1813.
22. K. M. Horsman, J. M. Bienvenue, K. R. Blasier and J. P. Landers, *J. Forensic Sci.*, 2007, **52**, 784–799.
23. A. Battaglia, A. J. Schweighardt and M. M. Wallace, *J. Forensic Sci.*, 2011, **56**, 760–765.
24. J. Cai, C. Yao, J. Xia, J. Wang, M. Chen, J. Huang, K. Chang, C. Liu, H. Pan and W. Fu, *Sensors Actuators B Chem.*, 2011, **155**, 500–504.

25. Z. Wang, T. Han, T. Jeon, S. Park and S. M. Kim, *Sensors Actuators B Chem.*, 2013, **178**, 683–688.
26. E. P. Randviir and C. E. Banks, *Anal. Methods*, 2013, **5**, 1098–1115.
27. M. E. Orazem and B. Tribollet, *Annu. Rev. Anal. Chem.*, 2010, **3**, 207–229.
28. L. Yang and R. Bashir, *Biotechnol. Adv.*, 2008, **26**, 135–150.
29. D. Mark, F. von Stetten and R. Zengerle, *Lab Chip*, 2012, **12**, 2464–8.
30. N. Ramanathan, M. Lukac, T. Ahmed, A. Kar, P. S. Praveen, T. Honles, I. Leong, I. H. Rehman, J. J. Schauer and V. Ramanathan, *Atmos. Environ.*, 2011, **45**, 4481–4487.
31. L. Yang and R. Bashir, *Biotechnol. Adv.*, 2008, **26**, 135–50.
32. E. Ferro and F. Potortì, *IEEE Wirel. Commun.*, 2005, **12**, 12–26.
33. D. A. Lytle, E. W. Rice, C. H. Johnson, K. R. Fox and K. I. M. R. Fox, *Appl. Environ. Microbiol.*, 1999, **65**, 3222–3225.
34. C. Ruan, L. Yang and Y. Li, *Anal. Chem.*, 2002, **74**, 4814–4820.
35. S. F. Altekruse, M. L. Cohen and D. L. Swerdlow, *Emerg. Infect. Dis.*, 1997, **3**, 285–293.
36. Y. Wang, Z. Ye and Y. Ying, *Sensors*, 2012, **12**, 3449–71.
37. M. Gandhi and M. L. Chikindas, *Int. J. Food Microbiol.*, 2007, **113**, 1–15.
38. C. Murphy, C. Carroll and K. N. Jordan, *J. Appl. Microbiol.*, 2006, **100**, 623–32.
39. V. Velusamy, K. Arshak, O. Korostynska, K. Oliwa and C. Adley, *Biotechnol. Adv.*, 2010, **28**, 232–54.
40. B. Swaminathan and P. Feng, *Annu. Rev. Microbiol.*, 1994, **48**, 401–426.
41. O. Lazcka, F. J. Del Campo and F. X. Muñoz, *Biosens. Bioelectron.*, 2007, **22**, 1205–17.
42. R. Y. C. Kong, S. K. Y. Lee, T. W. F. Law, S. H. W. Law and R. S. S. Wu, *Water Res.*, 2002, **36**, 2802–2812.
43. E. Leoni and P. P. Legnani, *J. Appl. Microbiol.*, 2001, **90**, 27–33.
44. X. Jiang, R. Wang, Y. Wang, X. Su, Y. Ying, J. Wang and Y. Li, *Biosens. Bioelectron.*, 2011, **29**, 23–8.
45. F. Tan, P. H. M. Leung, Z. Liu, Y. Zhang, L. Xiao, W. Ye, X. Zhang, L. Yi and M. Yang, *Sensors Actuators B Chem.*, 2011, **159**, 328–335.
46. E. P. Randviir and C. E. Banks, *Anal. Methods*, 2013, **5**, 1098.
47. C. J. Felice and M. E. Valentinuzzi, *IEEE Trans. Biomed. Eng.*, 1999, **46**, 1483–1487.
48. M. Varshney and Y. Li, *Biosens. Bioelectron.*, 2009, **24**, 2951–60.
49. R. Ehret, W. Baumann, M. Brischwein, A. Schwinde, B. Wolf and K. Stegbauer, *Biosens. Bioelectron.*, 1997, **12**, 29–41.
50. R. Hamada, H. Takayama, Y. Shonishi, L. Mao, M. Nakano and J. Suehiro, *Sensors Actuators B Chem.*, 2013, **181**, 439–445.
51. J. Suehiro, D. Noutomi, M. Shutou and M. Hara, *J. Electrostat.*, 2003, **58**, 229–246.
52. X. Li, D. R. Ballerini and W. Shen, *Biomicrofluidics*, 2012, **6**, 11301.
53. W. Dungchai, O. Chailapakul and C. S. Henry, *Anal. Chem.*, 2009, **81**, 5821–5826.
54. E. Carrilho, A. W. Martinez and G. M. Whitesides, *Anal. Chem.*, 2009, **81**, 7091–7095.
55. J. Jiang, X. Wang, R. Chao, Y. Ren, C. Hu, Z. Xu and G. L. Liu, *Sensors Actuators B Chem.*, 2014, **193**, 653–659.
56. F. Lisdat and D. Schäfer, *Anal. Bioanal. Chem.*, 2008, **391**, 1555–1567.

57. R. Buendia, F. Seoane and R. Gil-Pita, *J. Phys. Conf. Ser.*, 2010, **224**, 12126.
58. D. Rodbard, Y. Feldman, M. L. Jaffe and L. E. M. Miles, *Immunochemistry*, 1978, **15**, 77–82.
59. S. Kochowski and K. Nitsch, *Thin Solid Films*, 2002, **415**, 133–137.
60. A. Lasia, *Electrochemical Impedance Spectroscopy and Its Applications*, Springer, New York, 2014.
61. J. Suehiro, R. Yatsunami, R. Hamada and M. Hara, *J. Phys. D. Appl. Phys.*, 1999, **32**, 2814.
62. P. Nordlander, *Nat. Photonics*, 2008, **2**, 387–388.
63. H. A. Atwater and A. Polman, *Nat. Mater.*, 2010, **9**, 865–865.
64. T. Onodera and K. Toko, *Sensors*, 2014, **14**, 16586–16616.
65. A. J. Haes and R. P. Van Duyne, *Anal. Bioanal. Chem.*, 2004, **379**, 920–930.
66. X. F. Li and S. F. Yu, *Plasmonics*, 2010, **5**, 389–394.
67. B. Zargar and A. Hatamie, *Analyst*, 2012, **137**, 5334.
68. O. Nicoletti, F. de la Peña, R. K. Leary, D. J. Holland, C. Ducati and P. A. Midgley, *Nature*, 2013, **502**, 80–4.
69. S. Nie and S. R. Emory, *Science*, 1997, **275**, 1102–1106.
70. A. J. Chung, Y. S. Huh and D. Erickson, *Nanoscale*, 2011, **3**, 2903–2908.
71. Y. Luo, G. Wen, J. Dong, Q. Liu, A. Liang and Z. Jiang, *Sensors Actuators, B Chem.*, 2014, **201**, 336–342.
72. A. Liang, Z. Lu, Q. Liu, X. Zhang, G. Wen and Z. Jiang, *Rsc Adv.*, 2015, **5**, 5711–5715.
73. O. Péron, E. Rinnert, T. Toury, M. L. Chapelle and C. Compère, *Analyst*, 2011, **136**, 1018–1022.
74. A. A. Yanik, A. E. Cetin, M. Huang, A. Artar, S. H. Mousavi, A. Khanikaev, J. Connor, G. Shvets and H. Altug, *IEEE Photonic Soc. 24th Annu. Meet. PHO 2011*, 2011, **108**, 425–426.
75. M. R. Gartia, A. Hsiao, A. Pokhriyal, S. Seo, G. Kulsharova, B. T. Cunningham, T. C. Bond and G. L. Liu, *Adv. Opt. Mater.*, 2013, **1**, 68–76.
76. S. H. Lee, K. C. Bantz, N. C. Lindquist, S. H. Oh and C. L. Haynes, *Langmuir*, 2009, **25**, 13685–13693.
77. Z.-L. Yang, Q.-H. Li, B. Ren and Z.-Q. Tian, *Chem. Commun.*, 2011, **47**, 3909.
78. J. D. Caldwell, O. Glembocki, F. J. Bezares, N. D. Bassim, R. W. Rendell, M. Feygelson, M. Ukaegbu, R. Kasica, L. Shirey and C. Hosten, *ACS Nano*, 2011, **5**, 4046–4055.
79. A. Dhawan, M. Gerhold, A. Madison, J. Fowlkes, P. E. Russell, T. Vo-Dinh and D. N. Leonard, *Scanning*, 2009, **31**, 139–146.
80. M. R. Gartia, Z. Xu, E. Behymer, H. Nguyen, J. A. Britten, C. Larson, R. Miles, M. Bora, A. S.-P. Chang, T. C. Bond and G. L. Liu, *Nanotechnology*, 2010, **21**, 395701.
81. H. J. Park, M. Kang and L. J. Guo, *ACS Nano*, 2009, **3**, 2601–2608.
82. C. M. Hsu, S. T. Connor, M. X. Tang and Y. Cui, *Appl. Phys. Lett.*, 2008, **93**.
83. C. Ruan, G. Eres, W. Wang, Z. Zhang and B. Gu, *Langmuir*, 2007, **23**, 5757–5760.
84. M. Saito, A. Kitamura, M. Murahashi, K. Yamanaka, L. Q. Hoa, Y. Yamaguchi and E. Tamiya, *Anal. Chem.*, 2012, **84**, 5494–5500.
85. A. Gutes, I. Laboriante, C. Carraro and R. Maboudian, *J. Phys. Chem. C*, 2009, **113**, 16939–16944.

86. P. L. Stiles, J. A. Dieringer, N. C. Shah and R. P. Van Duyne, *Annu. Rev. Anal. Chem.*, 2008, **1**, 601–626.
87. S. Liu and X. Guo, *NPG Asia Mater.*, 2012, **4**, e23.
88. G. J. Nusz, S. M. Marinakos, A. C. Curry, A. Dahlin, F. Hook, A. Wax and A. Chilkoti, *Anal. Chem.*, 2008, **80**, 984–989.
89. B. Burr, F. A. Burr, K. H. Thompson, M. C. Albertson and C. W. Stuber, *Genetics*, 1988, **118**, 519–526.
90. M. Srisa-Art, E. C. Dyson, A. J. DeMello and J. B. Edel, *Anal. Chem.*, 2008, **80**, 7063–7067.
91. A. Holmberg, A. Blomstergren, O. Nord, M. Lukacs, J. Lundeberg and M. Uhlén, *Electrophoresis*, 2005, **26**, 501–510.
92. B. C. Galarreta, P. R. Norton and F. Lagugné-Labarthet, *Langmuir*, 2011, **27**, 1494–1498.
93. A. K. Singh, S. A. Khan, Z. Fan, T. Demeritte, D. Senapati, R. Kanchanapally and P. C. Ray, *J. Am. Chem. Soc.*, 2012, **134**, 8662–8669.
94. J. Jehlička, A. Culka, P. Vandenabeele and H. G. M. Edwards, *Spectrochim. Acta Part A Mol. Biomol. Spectrosc.*, 2011, **80**, 36–40.
95. Z. Xu, H.-Y. Wu, S. U. Ali, J. Jiang, B. T. Cunningham and G. L. Liu, *J. Nanophotonics*, 2011, **5**, 53526.
96. W. Dong, Y. Zhang, B. Zhang and X. Wang, *J. Raman Spectrosc.*, 2013, **44**, 1739–1745.
97. W. Dong, Y. Zhang, B. Zhang and X. Wang, *Anal. Methods*, 2012, **4**, 2772.
98. X. Wang, M. R. Gartia, J. Jiang, T.-W. Chang, J. Qian, Y. Liu, X. Liu and G. L. Liu, *Sensors Actuators B Chem.*, 2015, **209**, 677–685.
99. D. Zhang, Y. Lu, Q. Zhang, L. Liu, S. Li, Y. Yao, J. Jiang, G. L. Liu and Q. Liu, *Sensors Actuators B Chem.*, 2015, **222**, 994–1002.
100. D. Zhang, J. Jiang, J. Chen, Q. Zhang, Y. Lu, Y. Yao, S. Li, G. Logan Liu and Q. Liu, *Biosens. Bioelectron.*, 2015, **70**, 81–8.
101. J. Geng, C. Sun, J. Liu, L.-D. Liao, Y. Yuan, N. Thakor, J. Wang and B. Liu, *Small*, 2015, **11**, 1603–10.
102. M. Fleischmann, P. J. Herndra and A. J. McQuillan, *Chem. Phys. Lett.*, 1974, **26**, 163–166.
103. D.-P. Yang, S. Chen, P. Huang, X. Wang, W. Jiang, O. Pandoli and D. Cui, *Green Chem.*, 2010, **12**, 2038.
104. J. Geng, J. Liang, Y. Wang, G. G. Gurzadyan and B. Liu, *J. Phys. Chem. B*, 2011, **115**, 3281–8.
105. G. Das, F. Mecarini, F. Gentile, F. De Angelis, H. Mohan Kumar, P. Candeloro, C. Liberale, G. Cuda and E. Di Fabrizio, *Biosens. Bioelectron.*, 2009, **24**, 1693–9.
106. M. Kahl, E. Voges, S. Kostrewa, C. Viets and W. Hill, *Sensors Actuators B Chem.*, 1998, **51**, 285–291.
107. F. Ding, Z. Wang, S. He, V. M. Shalaev and A. V Kildishev, *ACS Nano*, 2015, **9**, 4111–4119.
108. Z. Xu, Y. Chen, M. R. Gartia, J. Jiang and G. L. Liu, *Appl. Phys. Lett.*, 2011, **98**, 241904.
109. L. Baia, M. Baia, J. Popp and S. Astilean, *J. Phys. Chem. B*, 2006, **110**, 23982–23986.
110. Z. Xu, M. R. Gartia, C. J. Choi, J. Jiang, Y. Chen, B. T. Cunningham and G. L. Liu, *J. Raman Spectrosc.*, 2011, **42**, 1939–1944.
111. T.-W. Chang, X. Wang, A. Hsiao, Z. Xu, G. Lin, M. R. Gartia, X. Liu and G. L. Liu, *Adv. Opt.*

Mater., 2015, **3**, 1397–1404.
112. C. J. Choi, Z. Xu, H.-Y. Wu, G. L. Liu and B. T. Cunningham, *Nanotechnology*, 2010, **21**, 415301.
113. Y. Peng, Y. He, S. Yang, S. Ben, M. Cao, K. Li, K. Liu and L. Jiang, *Adv. Funct. Mater.*, 2015, **25**, 5967–5971.
114. C. Yu, M. Cao, Z. Dong, J. Wang, K. Li and L. Jiang, *Adv. Funct. Mater.*, 2016, **26**, 3236–3243.
115. W. Chen, K. D. Long, M. Lu, V. Chaudhery, H. Yu, J. S. Choi, J. Polans, Y. Zhuo, B. A. C. Harley and B. T. Cunningham, *Analyst*, 2013, **138**, 5886–94.
116. Y. Zhuo, H. Hu, W. Chen, M. Lu, L. Tian, H. Yu, K. D. Long, E. Chow, W. P. King, S. Singamaneni and B. T. Cunningham, *Analyst*, 2014, **139**, 1007–15.
117. N. C. Lindquist, P. Nagpal, K. M. McPeak, D. J. Norris and S.-H. Oh, *Rep. Prog. Phys.*, 2012, **75**, 36501.
118. D. Zhang, Y. Lu, Q. Zhang, Y. Yao, S. Li, H. Li, S. Zhuang, J. Jiang, G. L. Liu and Q. Liu, *Sensors Actuators B Chem.*, 2015, **221**, 341–349.
119. D. Zhang, Y. Lu, J. Jiang, Q. Zhang, Y. Yao, P. Wang, B. Chen, Q. Cheng, G. L. Liu and Q. Liu, *Biosens. Bioelectron.*, 2015, **67**, 237–42.
120. Z. Xu, Y. Chen, M. R. Gartia, J. Jiang and G. L. Liu, *Appl. Phys. Lett.*, 2011, **98**, 241904.
121. C. Marambio-Jones and E. M. V. Hoek, *J. Nanoparticle Res.*, 2010, **12**, 1531–1551.
122. M. E. Hankus, D. N. Stratis-cullum and P. M. Pellegrino, in *SPIE-Optics and Photonics West*, 2011, vol. 8099, pp. 8099–7.
123. Z. Xu, J. Jiang, X. Wang, K. Han, A. Ameen, I. Khan, T.-W. Chang and G. L. Liu, *Nanoscale*, 2016, **8**, 6162–6172.
124. J. Homola, S. S. Yee and G. Gauglitz, *Sensors Actuators B Chem.*, 1999, **54**, 3–15.
125. K. A. Willets and R. P. Van Duyne, *Annu. Rev. Phys. Chem.*, 2007, **58**, 267–97.
126. J. Homola, *Anal. Bioanal. Chem.*, 2003, **377**, 528–39.
127. P. Pattnaik, *Appl. Biochem. Biotechnol.*, 2005, **126**, 79–92.
128. W. Dong, K. Pang, Q. Luo, Z. Huang, X. Wang and L. Tong, *Opt. Commun.*, 2015, **346**, 1–9.
129. B. Sepúlveda, P. C. Angelomé, L. M. Lechuga and L. M. Liz-Marzán, *Nano Today*, 2009, **4**, 244–251.
130. S. Zeng, D. Baillargeat, H.-P. Ho and K.-T. Yong, *Chem. Soc. Rev.*, 2014, **43**, 3426–52.
131. Y. Cui, Y. He, Y. Jin, F. Ding, L. Yang, Y. Ye, S. Zhong, Y. Lin and S. He, *Laser Photon. Rev.*, 2014, **8**, 495–520.
132. R. Nicolas, G. Lévêque, J. Marae-Djouda, G. Montay, Y. Madi, J. Plain, Z. Herro, M. Kazan, P.-M. Adam and T. Maurer, *Sci. Rep.*, 2015, **5**, 14419.